Accepted Manuscript

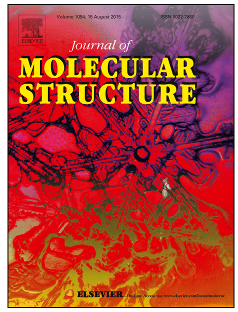

Synthesis, structural characterization and quantum chemical studies of silicon-containing benzoic acid derivatives

Mirela-Fernanda Zaltariov, Corneliu Cojocaru, Sergiu Shova, Liviu Sacarescu, Maria Cazacu

PII: S0022-2860(16)30484-7

DOI: 10.1016/j.molstruc.2016.05.038

Reference: MOLSTR 22552

To appear in: *Journal of Molecular Structure*

Received Date: 1 March 2016

Revised Date: 11 May 2016

Accepted Date: 12 May 2016

Please cite this article as: M.-F. Zaltariov, C. Cojocaru, S. Shova, L. Sacarescu, M. Cazacu, Synthesis, structural characterization and quantum chemical studies of silicon-containing benzoic acid derivatives, *Journal of Molecular Structure* (2016), doi: 10.1016/j.molstruc.2016.05.038.

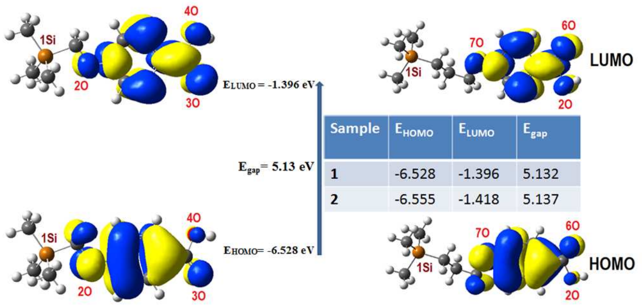

Sample	E_{HOMO}	E_{LUMO}	E_{gap}
1	-6.528	-1.396	5.132
2	-6.555	-1.418	5.137

4-((trimethylsilyl)methoxy)benzoic acid (1)

4-(3-(trimethylsilyl)propoxy)benzoic acid (2)

Synthesis, structural characterization and quantum chemical studies of silicon–containing benzoic acid derivatives

Mirela-Fernanda Zaltariov*, Corneliu Cojocaru, Sergiu Shova, Liviu Sacarescu, Maria Cazacu

Department of Inorganic Polymers, "Petru Poni" Institute of Macromolecular Chemistry, Romanian Academy, Aleea Grigore Ghica Voda 41 A, 700487 Iasi, Romania.

**Corresponding author*: Mirela-Fernanda Zaltariov

Email: zaltariov.mirela@icmpp.ro

Tel: +40-232-217454

Fax: +40-232-211299

Electronic Supplementary Information (ESI) available

Abstract

The present paper is concerned with the synthesis and molecular structure investigation of two new benzoic acid derivatives having trimethylsilyl tails, 4–((trimethylsilyl)methoxy) and 4–(3–(trimethylsilyl)propoxy)benzoic acids. The structures of the novel compounds have been confirmed by X–ray crystallography, Fourier–transform infrared spectroscopy (FTIR) and nuclear magnetic resonance (^{1}H and ^{13}C NMR). The theoretical studies of molecules were conducted by using the quantum chemical methods, such as Density Functional Theory (DFT B3LYP/6–31+G**), Hartree–Fock (HF/6–31+G**) and semiempirical computations (PM3, PM6 and PM7). The optimized molecular geometries have been found to be in good agreement with experimental structures resulted from the X–ray diffraction. The maximum electronic absorption bands observed at 272–287 nm (UV–vis spectra) have been assigned to $\pi \rightarrow \pi^*$ transitions, which were in reasonable agreement with the time dependent density functional theory (TD–DFT) calculations. The computed vibrational frequencies by DFT method were assigned and compared with the experimental FTIR spectra. The mapped electrostatic potentials revealed the reactive sites, which corroborated the observation of the dimer supramolecular structures formed in the crystals by hydrogen–bonding. The energies of frontier molecular orbitals (HOMO and LUMO), energy gap, dipole moment and molecular descriptors for the new compounds were calculated and discussed.

Keywords: Benzoic acid derivatives; Organosilicon compounds; Computational chemistry; Vibrational spectra; Electronic absorption spectra; HOMO–LUMO.

1. Introduction

Benzoic acid derivatives are versatile compounds used as chemicals, pharmaceuticals, agrochemicals and consumer products [1]. Benzoic acid inhibits bacterial development and its substituted compounds are very important for the development of new materials in food and pharmaceutical industries [2]. In the last years, considerable efforts have been devoted to theoretically and experimentally study of the benzoic acid derivatives [1–14]. Thus, a number of these compounds were investigated: *p*–hydroxybenzoic, *m*–anisic, vanillic, and syringic acids [1]; 4–butyl benzoic acid [2]; methyl– and methoxybenzoic acids [3]; *m*–trifluoromethylbenzoic acid [4]; 4–(2,5–di–2–thienyl–1H–pyrrol–1–yl)benzoic acid [5]; *p*–(*p*–hydroxyphenoxy)benzoic acid [6]; toluic acid [7]; 2–(4–hydroxyphenylazo)benzoic acid [8]; 2–amino–5–bromo–benzoic acid methyl ester [9]; 4–(trimethylammonium)benzoic acid chloride [10]; 2,3,4–tri–fluoro–benzoic acid dimer [11]; 2–[(2–hydroxyphenyl)carbonyloxy]benzoic acid [12]; Cu(II) complex with 4–{(Z)–[(2–hydroxybenzoyl)hydrazono]methyl}benzoic acid [13] and 4–[[(substituted phenyl)imino]methyl]benzoic acids [14]. All of the above mentioned molecules were mainly modeled by density functional theory (DFT), and the simulation outcomes were compared with the available experimental results (e.g. X–ray crystallography; FTIR, Raman, UV–vis and NMR spectra).

The current work aims to report on the synthesis pathway, molecular structure characterization and theoretical quantum chemical investigations of two novel benzoic acid derivatives having trimethylsilyl (TMS) tails, i.e. 4–((trimethylsilyl)methoxy) and 4–(3–(trimethylsilyl)propoxy)benzoic acids as potential ligands for the metal ions. The presence of TMS groups creates premises for obtaining metal complexes with increased solubility in non–polar media, such as supercritical carbon dioxide ($scCO_2$), a non–toxic, non–flammable, eco–friendly and relatively cheap solvent, where they can act as homogeneous catalyst for different reactions. The number of metal complexes that are soluble in this environment is very limited [15]. In addition, due to the higher hydrophobicity of the trimethylsilyl group, these compounds have a high potential for application as bioactive compounds in enzymatic reactions [16].

Previously published articles described the experimental investigations regarding the synthesis and characterization of benzoic acid derivatives containing organosilicon groups [17–19]. However, to the best of our knowledge no report has been focused, until now, on both theoretical and experimental investigations of the molecular structures of silicon–containing benzoic derivatives [20]. Molecular modeling is an extremely useful tool to complement experimental techniques providing a potential structural context for understanding the experimental results [21]. Note that, some organosilicon compounds have been tested as pharmaceuticals [20].

2. Experimental

2.1. Materials

4–Hydroxybenzoic acid (Aldrich), (chloromethyl)trimethylsilane 98% (Aldrich), (3–chlororpropyl)trimethylsilane 97% (Aldrich), anhydrous K_2CO_3 (Aldrich), Na_2SO_4 (Aldrich), dimethylformamide (Aldrich), chloroform (Aldrich) were used as received.

2.2. Methods

Fourier transform infrared (FT–IR) measurements were carried out using a Bruker Vertex 70 FT–IR spectrometer. Spectra were recorded in the transmission mode in the range 400–4000 cm^{-1} at room temperature with a resolution of 2 cm^{-1} and accumulation of 32 scans.

The NMR spectra were recorded on a Bruker Avance DRX 400 MHz Spectrometer equipped with a 5 mm QNP direct detection probe and Z–gradients. Spectra were recorded in $CDCl_3$, at room temperature. The chemical shifts are reported as δ values (ppm). The assignments of all the signals in the 1D NMR spectra were done using 2D NMR experiments like H,H–COSY, H,C–HMQC and H,C–HMBC.

UV–vis absorption spectra measurements were carried out in $CHCl_3$ and DMSO solutions on a Specord 200 spectrophotometer.

X–Ray crystallographic measurements for **1** and **2** were carried out with an Oxford–Diffraction XCALIBUR E CCD diffractometer equipped with graphite–monochromated Mo–Kα radiation. Single crystals were positioned at 40 mm from the detector and 848, and 208 frames were measured each for 25, and 40 s over 1° scan width for **1**, and **2**, respectively. The unit cell determination and data integration were carried out using the CrysAlis package of Oxford Diffraction [22]. The structures were solved by direct methods using Olex2 [23] and refined by full–matrix least–squares on F^2 with SHELXL–97 [24]. Atomic displacements for non–hydrogen atoms were refined using an anisotropic model. All H atoms were introduced in idealized positions (dCH = 0.96 Å) using the riding model with their isotropic displacement parameters fixed at 120% of their riding atom. The molecular plots were obtained using the Olex2 program. The crystallographic data and refinement details are quoted in Table 1, while bond lengths, interatomic angles and dihedral angles are summarized in ESI (**Tables B1-B6**).

Table 1. Crystallographic data and structure refinement parameters for the compounds **1** and **2**.

Compound	**1**	**2**
Empirical formula	$C_{11}H_{16}O_3Si$	$C_{13}H_{20}O_3Si$
Formula weight	224.331 g/mol	252.385 g/mol
Temperature	200.00(14) °K	200.05(10) °K
Crystal system	triclinic	monoclinic
Space group	P-1	$P2_1/c$

Unit cell dimensions	a = 6.6120(3) Å b = 7.6894 (4) Å c = 12.8140(10) Å 101.928(6)° 98.644(6)° 100.425(4) °	a = 16.508(13) Å b = 10.026(2) Å c = 8.8482(15) Å 90.00° 95.89(3)° 90.00°
Volume	614.86(6) $Å^3$	1456.8(12) $Å^3$
Z	2	4
Calculated density	1.212 g/cm^3	1.151 g/cm^3
Absorption coefficient, μ	0.177 mm^{-1}	0.156 mm^{-1}
F(000)	240.0	544.0
Crystal size	0.15 × 0.1 × 0.1 mm	0.1 × 0.05 × 0.05 mm
Radiation (wavelength)	MoKα (λ = 0.71073 Å)	MoKα (λ = 0.71073 Å)
2Θ range for data collection	5.54 to 46.5°	4.76 to 46.5°
Index ranges	$-7 \leq h \leq 7$, $-8 \leq k \leq 8$, $-14 \leq l \leq 14$	$-12 \leq h \leq 18$, $-11 \leq k \leq 11$, $-9 \leq l \leq 9$
Reflections collected	5839	4770
Independent reflections	1736 [R_{int} = 0.0334, R_{sigma} = 0.0303]	2080 [R_{int} = 0.0568, R_{sigma} = 0.1031]
Data/restraints/parameters	1736/0/140	2080/0/158
Goodness-of-fit (GOF) on F^2	1.064	1.051
Final R indexes [I>=2σ (I)]	R_1 = 0.0897, wR_2 = 0.2172	R_1 = 0.0933, wR_2 = 0.1862

Final R indexes [all data]	R_1 = 0.0931, wR_2 = 0.2187	R_1 = 0.1745, wR_2 = 0.2275
Largest diff. peak and hole	0.88 and -0.38 e Å^{-3}	0.34 and -0.25 e Å^{-3}

$R_1 = \Sigma||F_o| - |F_c||/\Sigma|F_o|$;

$wR_2 = \{\Sigma[w(F_o^2 - F_c^2)^2]/\Sigma[w(F_o^2)^2]\}^{1/2}$;

GOF = $\{\Sigma[w(F_o^2 - F_c^2)^2]/(n - p)\}^{1/2}$, where n is the number of reflections and p is the total number of parameters refined.

CCDC–1438222 (**1**), CCDC–1438223 (**2**) contain the supplementary crystallographic data for this contribution. These data can be obtained free of charge via www.ccdc.cam.ac.uk/conts/retrieving.html (or from the Cambridge Crystallographic Data Centre, 12 Union Road, Cambridge CB2 1EZ, UK; fax: (+44) 1223-336-033; or deposit@ccdc.ca.ac.uk).

2.3. Synthesis

*2.3.1. Synthesis of **1***

In a 100 mL round bottom flask equipped with magnetic stirring and reflux condenser protected with $CaCl_2$ tube, 4–hydroxybenzoic (0.98 g, 7 mmol) and (trimethylsilyl)chlorometylsilane (0. 86 g, 1 mL, 7 mmol) were disolved together in DMF (15 mL). Anhydrous K_2CO_3 (1.45 g, 10.5 mmol) was added to the resulting solution and the mixture was stirred under argon athmosphere at 110 ^{o}C for 8 hours. The resulting precipitate was filtered off and the filtrate was poured into water (60 mL) and extracted with chloroform (3 x 15 mL). The combined organic phases were dried (Na_2SO_4) and evaporated under reduced pressure. The resulted beige solid product was dried in vacuo. X–ray diffraction–quality single crystals were obtained by recrystallization from methanol, washed with methanol and diethylether and dried in air at room temperature. Yield: 1.2 g, 75%. Anal. Calcd for $C_{11}H_{16}O_3Si$ (M_r 224.33): C, 58.89, H, 7.19. Found: C, 58.67, H, 7.23.

IR ν_{max} (KBr), cm^{-1}: 3551w, 3474w, 3416w, 2957w, 2901w, 2882w, 2822w, 1688s, 1601vs, 1578s, 1506s, 1421m, 1292s, 1250s, 1215m, 1157s, 1130vw, 1109w, 1007m, 858vs, 847vs, 775m, 758w, 706w, 636m, 619m, 604w, 546w, 513w, 505w, 480vw, 451vw, 378vw.

^{1}H NMR ($CDCl_3$, 400.13 MHz, δ, ppm): 9.87 (s, 1H, –COO*H*), 7.82 (d, *J*=8.7 Hz, 2H, Ar–*H*), 7.05 (d, *J*=8.7 Hz, 2H, Ar–*H*), 3.66 (s, 2H,–C*H*$_2$–), 0.16 (s, 9H, –Si–C*H*$_3$).

^{13}C NMR ($CDCl_3$, 100.16 MHz, δ, ppm): 190.88 (–*C*OOH), 166.72 (Ar–*C*), 131.91 (Ar–*C*), 129.63 (Ar–*C*), 114.53 (Ar–*C*), 61.78 (–*C*H$_2$–), –3.20 (–Si–*C*H$_3$).

UV–vis ($CHCl_3$), λ_{max} (ε, L $M^{-1}cm^{-1}$): 272 (21816); UV–vis (DMSO), λ_{max} (ε, L $M^{-1}cm^{-1}$): 275 (20823).

2.3.2. Synthesis of ***2***

In a 100 mL round bottom flask equipped with magnetic stirrer and reflux condenser protected with $CaCl_2$ tube, 4–hydroxybenzoic (0.83 g, 6 mmol) and (trimethylsilyl)chloropropylsilane (0. 88 g, 1 mL, 6 mmol) were disolved together in DMF (15 mL). Anhydrous K_2CO_3 (1.45 g, 10.5 mmol) was added to the resulting solution and the mixture was stirred under argon athmosphere at 110 ^oC for 8 hours. The resulting precipitate was filtered off and the filtrate was poured into water (60 mL) and extracted with chloroform (3 x 15 mL). The combined organic phases were dried (Na_2SO_4) and evaporated under reduced pressure. The solid product was dried in vacuo. X–ray diffraction–quality single crystals were obtained by recrystallization from chloroform/methanol (1:2, v:v), washed with methanol and diethylether and dried in air at room temperature. Yield: 1.3 g, 86 %. Anal. Calcd for $C_{11}H_{16}O_3Si$ (M_r 252.38): C, 61.87, H, 7.99. Found: C, 61.67, H, 8.13.

IR ν_{max} (KBr), cm^{-1}: 3366m, 3289m, 3155w, 3119w, 3074m, 3040w, 2951vs, 2895s, 2878s, 2826s, 2904s, 2735s, 2573w, 2515vw, 2428vw, 2012w, 1936vw, 1906w, 1693vs, 1601vs, 1578vs, 1510vs, 1470s, 1427s, 1393s, 1313s, 1250vs, 1215vs, 1184s, 1159vs, 1109s, 1063s, 1047s, 1009s, 895s, 854vs, 835vs, 787s, 758s, 694s, 650s, 617s, 606s, 515s, 453w, 436w, 422w, 382w.

^{1}H NMR ($CDCl_3$, 400.13 MHz, δ, ppm): 9.86 (s, 1H, –COO*H*), 7.82 (d, *J*=8.7 Hz, 2H, Ar–*H*), 6.97 (d, *J*=8.7 Hz, 2H, Ar–*H*), 3.98 (t, *J*=6.8 Hz, –CH_2–CH_2–CH_2–), 1.84–1.77 (m, 2H, –CH_2–CH_2–CH_2–), 0.63–0.58 (m, 2H, –CH_2–CH_2–CH_2–), 0.02 (s, 9H, –Si–CH_3).

^{13}C NMR ($CDCl_3$, 100.16 MHz, δ, ppm): 190.85 (–*C*OOH), 164.24 (Ar–*C*), 132.00 (Ar–*C*), 129.68 (Ar–*C*), 114.72 (Ar–*C*), 70.99 (–CH_2–CH_2–CH_2–), 23.66 (–CH_2–*C*H_2–CH_2–), 12.50 (–CH_2–CH_2–*C*H_2–), –1.79 (–Si–*C*H_3).

UV–vis ($CHCl_3$), λ_{max} (ε, L M^{-1}cm^{-1}): 285 (28235); UV–vis (DMSO), λ_{max} (ε, L M^{-1}cm^{-1}): 287 (26176).

3. Results and discussion

A reaction of Williamson type was used to prepare two silicon–containing dicarboxylic acids by treating 4–hydroxybenzoic acid with (chloromethyl)trimethylsilane and (3–chlororpropyl)trimethylsilane, respectively in 1:1 molar ratio, in DMF, in the presence of K_2CO_3 (**Figure 1**). This is a S_N2 reaction between the deprotonated alcohol and the alkyl halide moiety attached to the silicon atom. The alcohol deprotonation occurs *in situ* in the presence of K_2CO_3. The reaction products were isolated in pure, crystalline state, in reasonable yields (75 and 86 wt%, respectively).

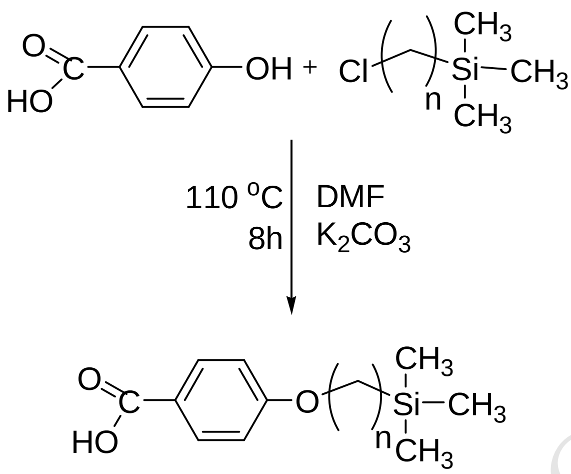

n=1, **(1)**; n=3, **(2)**

Figure 1. Scheme of the synthesis route of the titled compounds,

(n=1): 4–((trimethylsilyl)methoxy)benzoic acid;

(n=3): 4–(3–(trimethylsilyl)propoxy)benzoic acid.

The ^{1}H NMR and ^{13}C NMR spectra of the silicon–containing carboxylic acids are given in ESI (**Figures C1–C4)**. The ^{1}H NMR spectrum of **1** confirms the proposed structure by the presence of the four aromatic protons at 7.82 and 7.05 ppm, a singlet for the carboxylic acid proton at 9.87 ppm, a singlet assigned to –CH_2–O– at 3.66 ppm, while the peak corresponding to –Si–CH_3 protons appears at 0.16 ppm. The ^{13}C NMR spectrum is also in concordance with the proposed structure.

In the ^{1}H NMR spectrum of **2**, all protons resonated at appropriate positions: a singlet for carboxylic acid proton at 9.86 ppm, doublets for aromatic protons at 7.82 ppm and 6.97 ppm, while the aliphatic protons and those of the trimethylsilyl groups appear in the region 3.98-0.58 ppm and at 0.02 ppm respectively. Their intensity ratio corresponds with the presumed structure. The ^{13}C NMR spectra also confirm their structure (ESI, **Figures C2 and C4**).

3.1. X–ray crystallography

The molecular structures determined by X–ray crystallography are given as ORTEP plots with the atom–numbering scheme in **Figure 2**.

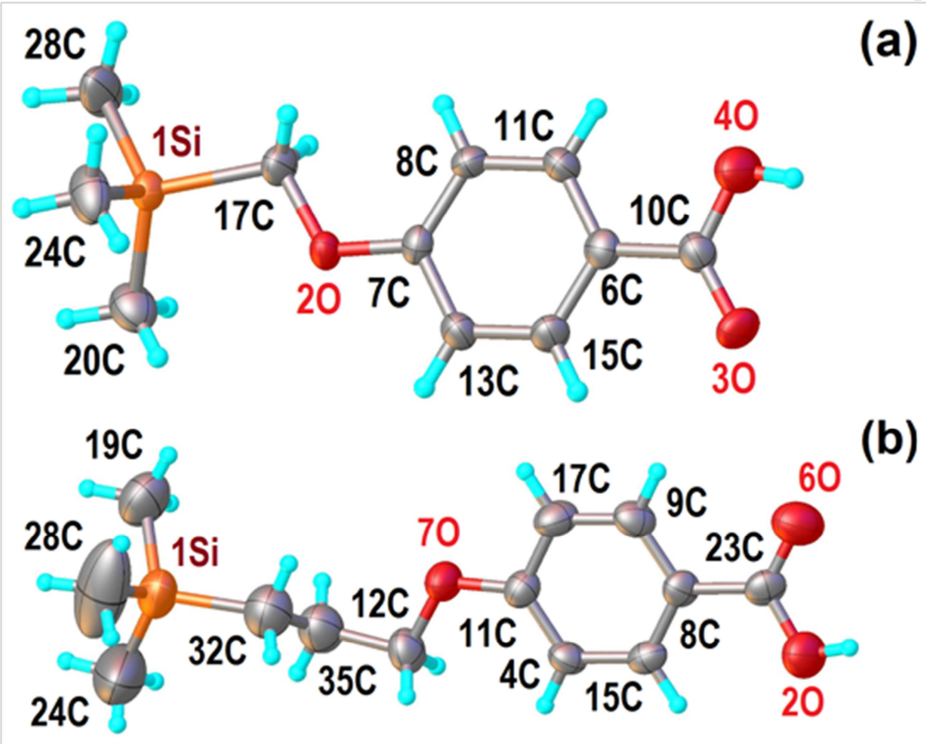

Figure 2. Molecular structures of the investigated compounds determined by X–ray structure analysis (Olex2 view): (**a**) **1** ($C_{11}H_{16}O_3Si$), 4–((trimethylsilyl)methoxy)benzoic acid; (**b**) **2** ($C_{13}H_{20}O_3Si$), 4–(3–(trimethylsilyl)propoxy)benzoic acid. Thermal ellipsoids are drawn at 50% probability level.

The single–crystal X–ray study has revealed that both compounds have molecular crystal structures resulted from the packing of dimeric supramolecular architectures, by formation of the stable cyclic hydrogen bonded system, as depicted in **Figure 3**. No co–crystallized solvent has been found in the crystals of compounds **1** and **2**.

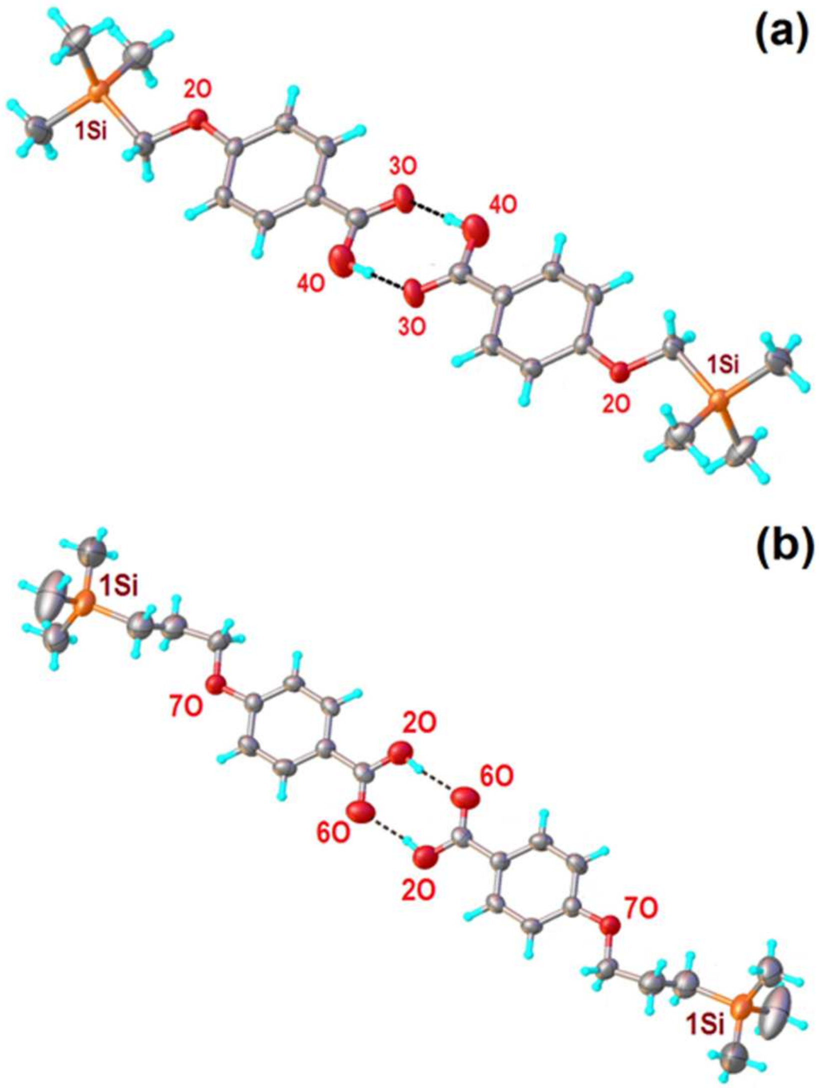

Figure 3. Partial packing diagrams for the compounds **1** (a) and **2** (b) showing the dimmers structures formed via hydrogen-bond bridges (O…H-O). Thermal ellipsoids are drawn at 50% probability level. H-bonds parameters of **1**.: O4−H···O3 [O4−H 0.82 Å, H···O3 1.83 Å, O4···O3 (3 – *x*, 3 - *y*, 1 - *z*) 2.625(6) Å, O4−H···O3 161.5°]. H-bonds parameters of **2**: O2−H···O6 [O2−H 0.82 Å, H···O6 1.80 Å, O2···O6 (2 – *x*, 1 - *y*, 2 - *z*) 2.613(6) Å, O2−H···O6 171.0°].

Apart from the H–bonding, in the crystal of **1**, the system of intermolecular interactions is completed by the significant π–π stacking between centrosymmetrically related C6–C15 aromatic rings, which is evidenced by the centroid–to–centroid distance of 3.723 Å and shift distance of 1.364 Å. These interactions are responsible for the supramolecular aggregation of the dimeric units into the ribbon–like architecture running parallel to [110] direction (ESI, **Figure A1**).

4. Computational details

The silicon–containing benzoic acid derivatives **1** and **2** were modeled by computational chemistry approach using the density functional theory (DFT), ab–initio (Hartree–Fock, HF) and semiempirical (PM3, PM6 and PM7) methods. To this end, the quantum chemical calculations (DFT, HF and semiempirical) were performed in order to study the molecular structure characteristics and electronic properties of the titled compounds. The software package Gaussian 09 [25] was employed for DFT and HF calculations of the molecules, using the split–valence basis set 6–31+G** with added polarization and diffuse functions. The density functional method was implemented at the level of B3LYP functional (i.e. B3LYP/6-31+G**). The computations by PM3, PM6 and PM7 methods were performed by means of MOPAC semiempirical quantum chemistry program [26–31]. The molecular modeling results were analyzed using graphical–interface computational chemistry software, such as GaussView 5 [32], Gabedit [33] and HyperChem [34].

Geometry optimization is an important part of computational chemistry, and it deals with searching by energy minimization of the optimized molecular structures [35]. In this work, the geometry optimization of molecules **1** and **2** was performed by minimizing the energies with respect to all geometrical parameters without imposing any symmetry constrains. The input structures for optimization were taken from the CIF–files obtained from X–ray single–crystal measurements. Further, the geometry optimization was performed on single molecules, in vacuo.

Frequency calculations at the optimized geometries were done to confirm the optimum conformations (i.e. no imaginary frequencies) and to analyze the vibration modes. The electronic absorption spectra of the investigated compounds were calculated by the time dependent density functional theory (TD–DFT).

4.1. Optimized molecular structures

Since the properties of a molecule depend on its structure, an important goal in computational chemistry is to find the most probable geometry of the molecule by optimization.

In this work, the molecular geometries of the investigated acids **1** and **2** were optimized at different theoretical levels using B3LYP/6–31+G**, HF/6–31+G** as well as semiempirical (PM3, PM6 and PM7) methods. **Figure 4** illustrates as an example, the optimized geometries of compounds **1** and **2** computed by B3LYP/6–31+G** method. The ball and stick rendering models with full atomic numbering have been used for the spatial representations. The investigated compounds possess C_1 symmetry (point group).

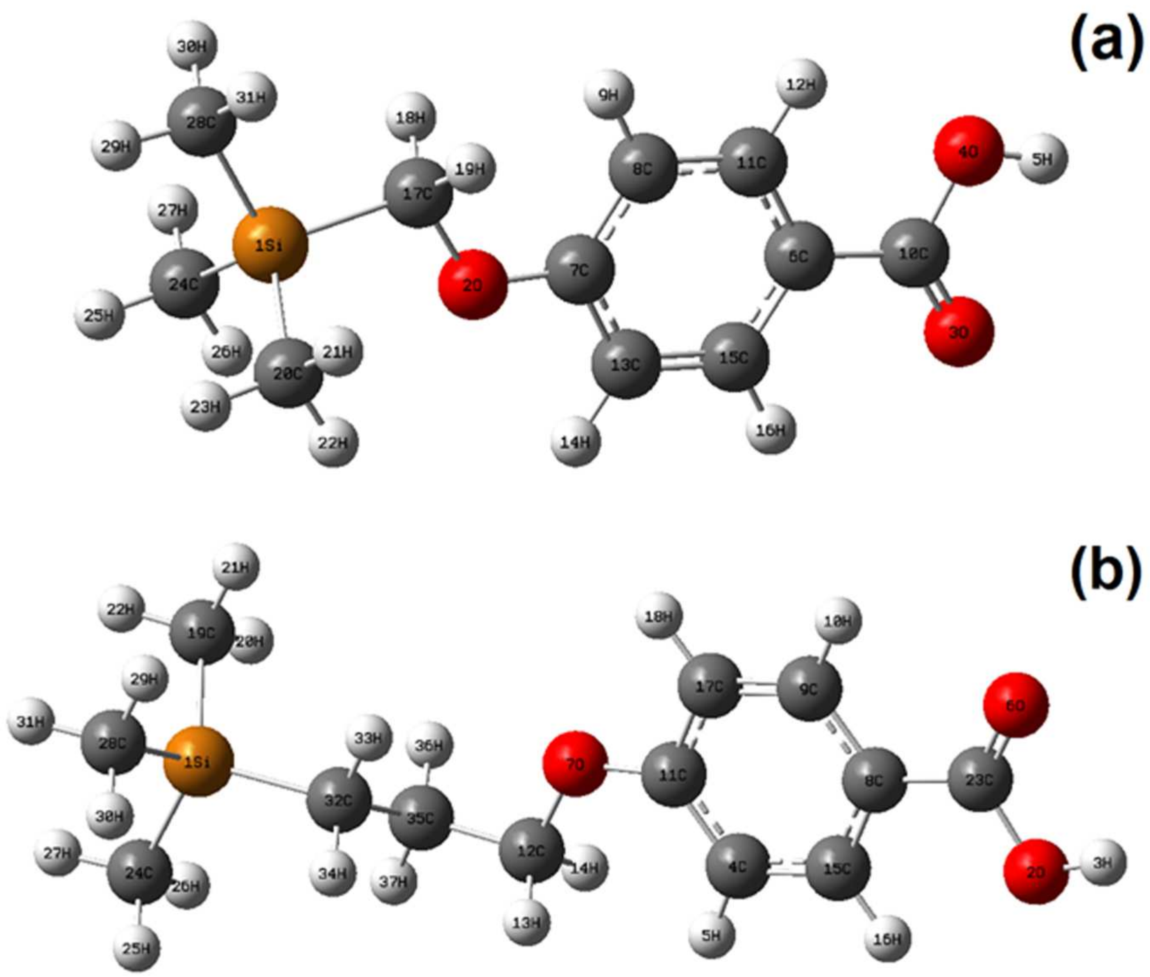

Figure 4. Optimized molecular geometries of the investigated compounds **1** (a) and **2** (b), computed at ground state (S_0) by DFT method (B3LYP/6–31+G**); balls and sticks rendering models with full atomic numbering.

The optimized structure parameters such as bond lengths, interatomic angles and dihedrals of the studied compounds were calculated by computational chemistry methods and compared with the experimental values observed from X–ray crystallography. The full analysis of the optimized structure parameters and the corresponding experimental counterparts is given in the *electronic supplementary information* ESI (**Tables B1–B6**). The representative geometric parameters are summarized in **Table 2**.

Table 2. Summary of selected structural parameters: bond lengths (Å), angles (^{o} deg) and dihedrals (^{o} deg), for the investigated molecules **1** ($C_{11}H_{16}O_3Si$) and **2** ($C_{13}H_{20}O_3Si$).

Geometry: **1**	Exp. [a]	PM3	PM6	PM7	HF [b]	DFT [c]
1Si-17C	1.884(6)	1.936	1.924	1.898	1.911	1.918
1Si-28C	1.849(8)	1.888	1.865	1.866	1.891	1.892
2O-7C	1.358(8)	1.376	1.362	1.350	1.340	1.360
2O-17C	1.436(7)	1.412	1.465	1.431	1.419	1.440
17C-1Si-28C	106.3(3)	105.649	103.611	106.251	106.789	106.730
7C-2O-17C	118.8(4)	116.844	118.130	117.644	121.103	119.777
1Si-17C-2O	109.0(4)	109.061	112.740	105.145	108.136	108.179
28C-1Si-17C-2O	166.0(5)	178.079	179.632	179.761	-179.971	-179.954
7C-2O-17C-1Si	170.8(4)	162.090	179.488	179.255	-179.927	-179.934
Geometry: 2	**Exp.**	**PM3**	**PM6**	**PM7**	**HF**	**DFT**
1Si-24C	1.821(10)	1.890	1.870	1.870	1.892	1.894
1Si-32C	1.907(7)	1.908	1.892	1.886	1.900	1.905
7O-11C	1.362(6)	1.371	1.361	1.348	1.338	1.358
7O-12C	1.440(6)	1.425	1.469	1.435	1.411	1.434
28C-1Si-32C	106.8(4)	108.426	107.118	107.665	108.213	108.324
11C-7O-12C	117.1(4)	117.410	118.917	118.063	120.932	119.492
12C-35C-32C	114.5(6)	112.885	110.199	109.833	113.913	114.186
28C-1Si-32C-35C	171.7(6)	-179.584	179.051	-179.832	179.342	-179.319

11C-7O-12C-35C	-179.2(5)	178.110	179.968	177.023	179.312	179.062

Histograms have been ploted on the basis of complete analysis of structure parameters (**Tables B1–B6**) and following the approach proposed in Refs. [36,37] the histograms have been plotted as shown in **Figure 5.** Such histograms give the general image concerning the distributions of the bond lengths and interatomic angles in the molecule based on experimental observations and theoretical results. As shown in **Figure 5**, some models overestimate whereas others underestimate in reasonable limits the observed structural parameters of the studied molecules.

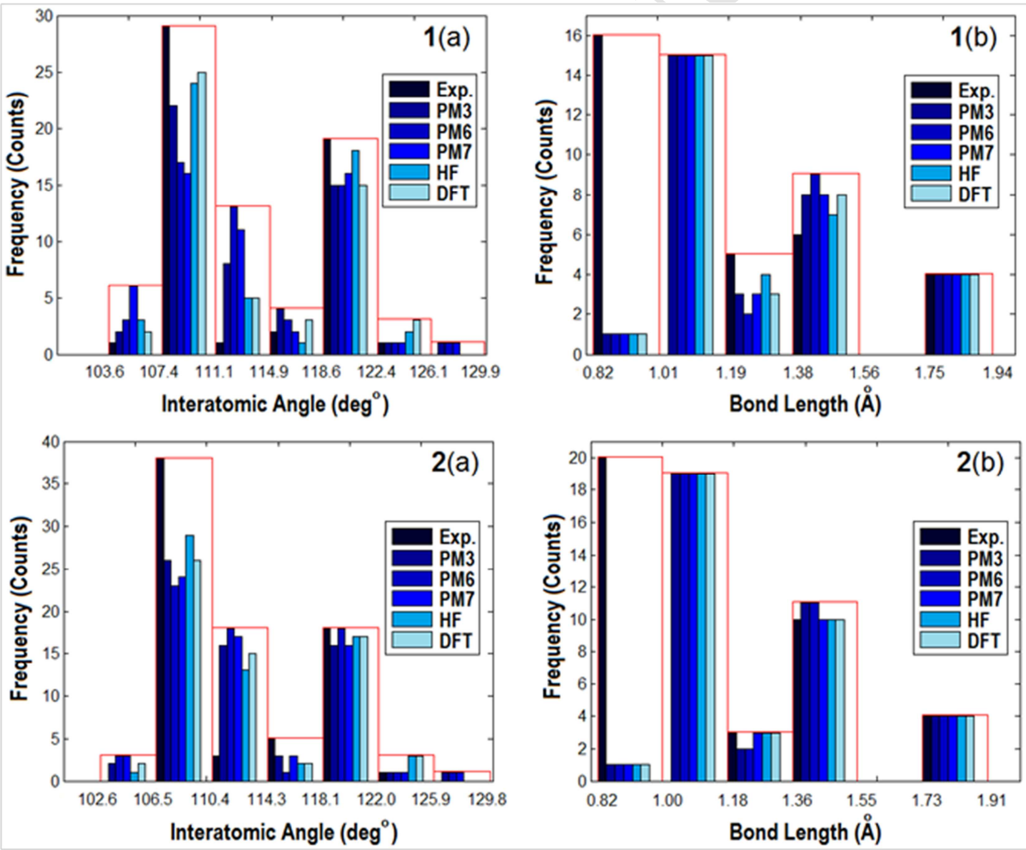

Figure 5. Histograms of interatomic angles distributions (a) and bond lengths distributions (b) for the investigated compounds **1** and **2**.

All theoretical models overestimated the shortest bond lengths values for O–H and C–H. As presented in histograms (**Figure 5**), the highest frequencies for these bonds were within 0.82–1.19 Å range. For Si–C, C–O, C=O and C–C both the calculated and measured bond lengths were in good agreement (**Figure 5** and **Tables B1, B4 /** ESI).

All values of interatomic angles for the studied benzoic acid derivatives are reported in **Tables B2** and **B5** (ESI). **Figure 5** also shows the histograms of interatomic angles distributions plotted on the basis of experimental data and theoretical models. As shown in **Table 2** the bond angles are reasonable predicted by the quantum chemistry models.

Some structural disparities have been observed in terms of torsion angles (dihedrals). The information about dihedrals (torsion angles) for **1** and **2** is given extensively in **Tables B3** and **B6** (ESI), respectively. In **Table 2** only the selected torsion angles are summarized.

Such differences could be explained by taking into account the conformational constraints that occur when the molecules are assembled in crystalline structures. However, in order to identify the overall conformational similitude between observed molecular structures and the modeled ones, the overlap plots and the calculation of root–mean–square–deviation (*RMSD*) are commonly used as goodness–of–fit estimators [38–40]. The *RMSD* [40] of the atomic positions is a similarity measure for the quantitative comparison of one structure with another, and it is given by:

$$RMSD(\mathbf{r}) = \sqrt{\frac{1}{N}\sum_{k=1}^{N}\left(\mathbf{r}_k^{(i)} - \mathbf{r}_k^{(j)}\right)^2} \tag{1}$$

Where N denotes the number of atoms in the molecule; k is an index over these atoms; $\mathbf{r}_k^{(i)}$, $\mathbf{r}_k^{(j)}$ – coordinates of atom k in conformations i and j. The minimal value of *RMSD* is desirable and it is obtained by the optimal superposition of the two structures. In this work, the *RMSD* values have been calculated to compare the observed molecular structures (from X–ray crystallography) with their optimized geometries given by quantum chemistry models. The calculated values of *RSMD* are summarized in **Table 3**.

Table 3. Root mean square deviation (RMSD) values to compare the goodness–of–fit between observed and predicted structures of the investigated molecules **1** and **2**.

	PM3	PM6	PM7	HF	DFT
1 ($C_{11}H_{16}O_3Si$)					
RMSD, Å	0.2553	0.4304	0.4173	0.4151	0.4212
2 ($C_{13}H_{20}O_3Si$)					
RMSD, Å	0.2029	1.4959	0.3499	0.2328	0.2302

In addition, the overlap plots are given in **Figure 6** and ESI (**Figures A2–A3**), showing the superposition of the X–ray structures of the compounds and their optimized counterparts. Generally, the predicted geometries are quite similar with the experimental molecular structures (**Figure 6** and **Figures A2–A3**/ESI).

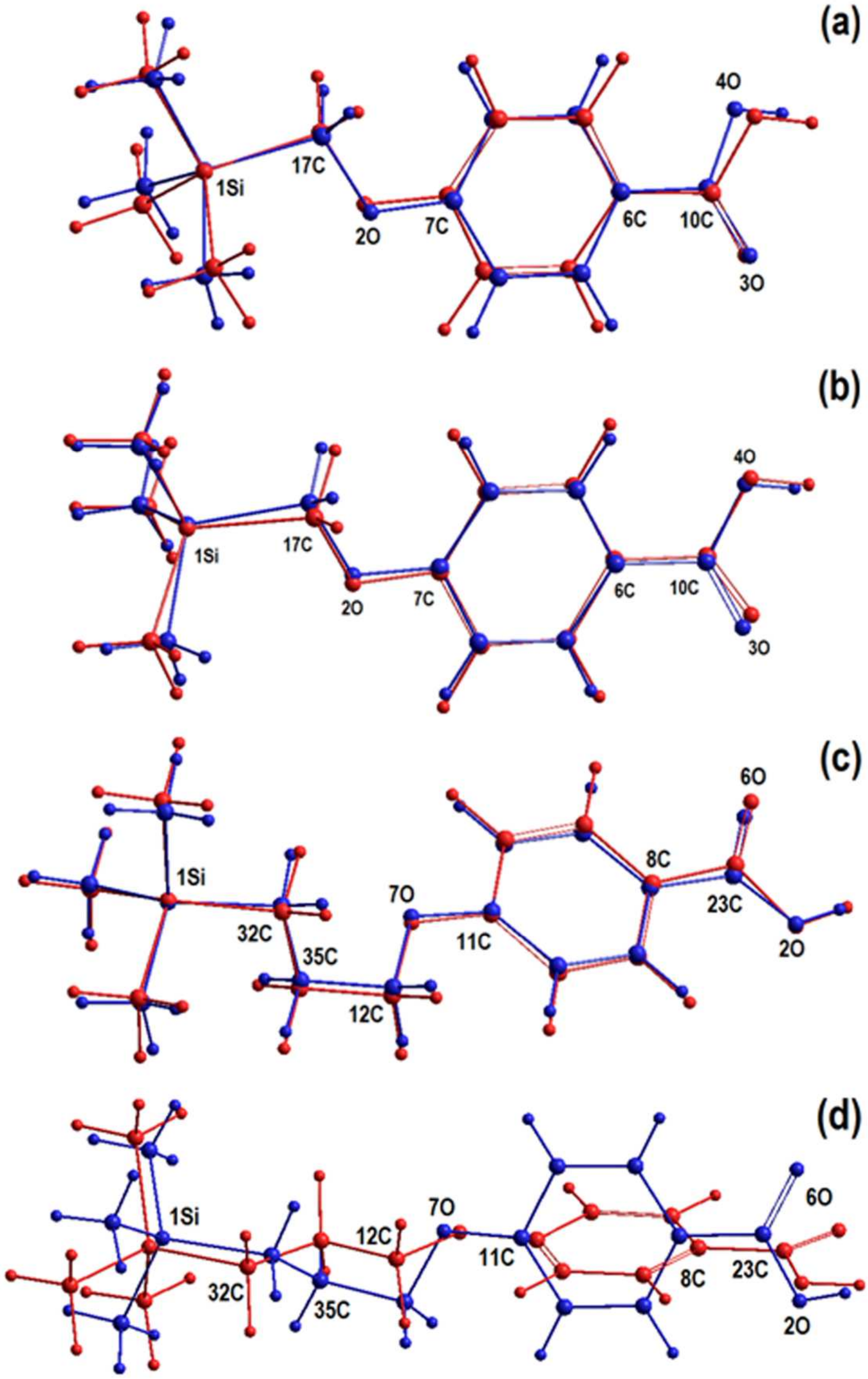
(a)
4O
1Si
17C
2O
7C
6C
10C
3O
(b)
4O
1Si
17C
2O
7C
6C
10C
3O
(c)
6O
1Si
8C
7O
23C
32C
11C
35C
2O
12C
(d)
1Si
7O
6O
12C
11C
32C
35C
8C
23C
2O

Figure 6. Superposition of the X–ray structures (blue) of the investigated compounds and their optimized counterparts (red) computed by different methods: (a) **1** (HF/6–31+G**); (b) **1** (PM3); (c) **2** (B3LYP/6–31+G**); (d) **2** (PM6).

The semiempirical method PM3 has yield the lowest *RSMD* values of 0.2553 Å and 0.2029 Å (**Table 3**), for the compounds **1** and **2**, respectively, showing the best similitude with the observed structures. This may be attributed to the fact that PM3 method has better predicted the dihedral angles. Likewise, the methods HF, DFT and PM7 were appropriate for the optimization of molecular structures of the benzoic–acid derivatives, providing the low values of *RMSD*, i.e. *RMSD*<0.43 Å (**Table 3**). The semiempirical method PM6 indicated the greatest values of *RMSD*, suggesting some conformational discrepancy between modeled structures and observed ones. For example, in case of compound **2**, the *RMSD* value given by PM6 method is equal to 1.4959 Å, which is significantly greater than *RMSD* values provided by the other methods. This structural disparity in terms of atomic positions can be also seen in **Figure 6** (d). In summary, the optimized molecular geometries computed by DFT, HF, PM3 and PM7 methods were in good agreement with the observed molecular structures obtained from X–ray crystallography. In turn, the optimized geometries calculated by PM6 method fairly matched with the observed structures.

4.2. Molecular orbital analysis and electronic properties

The molecular orbital (MO) analysis is extensively employed to describe the electronic structure and chemical behavior of the investigated molecule. The theoretical results concerning the modeled molecules **1** and **2** are summarized in **Tables 4** and **5**, respectively. This information refers to the optimized molecular electronic structures of the investigating compounds. Thus, **Tables 4** and **5** provide theoretical outcomes regarding the number of double occupied molecular orbitals treated by quantum chemistry methods; total energy; dipole moment; molecular size; energies of frontier molecular orbitals; band gap energy and molecular descriptors.

Table 4. Summary of theoretical results obtained for optimized geometries of the investigated molecule **1** ($C_{11}H_{16}O_3Si$) using different QM methods.

	DFT	HF	PM3	PM6	PM7
No. of occ. MO	60	60	41	41	41
E_t, (kcal / mol)	-592411	-589522	-57765	-57958	-58936
μ_D, (Debye)	4.324	4.131	3.968	6.093	4.674
d_{max}, (Å)	11.967	11.909	11.812	11.598	11.865
S_m, (Å^2)	458.61	454.29	464.16	462.98	456.92
V_m, (Å^3)	735.71	730.11	734.35	734.84	730.44
$E_{\text{LUMO+1}}$ (eV)	-0.623	1.697	0.163	0.124	-0.039
E_{LUMO} (eV)	-1.396	1.212	-0.324	-0.347	-0.412
E_{HOMO} (eV)	-6.528	-8.851	-9.287	-9.117	-9.310
$E_{\text{HOMO-1}}$ (eV)	-7.332	-9.587	-10.534	-10.172	-10.285
ΔE, (eV)	5.132	10.063	8.963	8.770	8.898
ΔE_1 , (eV)	6.709	11.284	10.697	10.296	10.246
IP (eV)	6.528	8.851	9.287	9.117	9.310
EA (eV)	1.396	-1.212	0.324	0.347	0.412
χ (eV)	3.962	3.820	4.806	4.732	4.861
μ (eV)	-3.962	-3.820	-4.806	-4.732	-4.861

η (eV)	2.566	5.032	4.482	4.385	4.449
ω (eV)	3.059	1.450	2.576	2.553	2.656

Table 5. Summary of theoretical results obtained for optimized geometries of the investigated molecule **2** ($C_{13}H_{20}O_3Si$) using different QM methods.

	DFT	HF	PM3	PM6	PM7
No. of occ. MO	68	68	47	47	47
E_t, (kcal / mol)	-641757	-638518	-64663	-64873	-65853
μ_D, (Debye)	4.098	3.937	3.645	5.674	4.329
$d_{\max}$, (Å)	13.946	13.892	13.869	14.410	13.814
S_m, (Å^2)	522.38	515.47	520.50	520.46	511.10
V_m, (Å^3)	837.37	831.29	833.35	838.23	832.64
$E_{\text{LUMO+1}}$ (eV)	-0.647	1.643	0.088	-0.009	-0.088
E_{LUMO} (eV)	-1.418	1.311	-0.388	-0.472	-0.459
E_{HOMO} (eV)	-6.555	-8.878	-9.406	-9.307	-9.384
$E_{\text{HOMO-1}}$ (eV)	-7.358	-9.616	-10.156	-9.984	-10.332
ΔE, (eV)	5.137	10.189	9.018	8.835	8.925
ΔE_1 , (eV)	6.711	11.259	10.244	9.975	10.244
IP (eV)	6.555	8.878	9.406	9.307	9.384
EA (eV)	1.418	-1.311	0.388	0.472	0.459
χ (eV)	3.986	3.784	4.897	4.890	4.922
μ (eV)	-3.986	-3.784	-4.897	-4.890	-4.922

η (eV)	2.568	5.095	4.509	4.418	4.463
ω (eV)	3.094	1.405	2.659	2.706	2.714

According to the theoretical results listed in **Tables 4** and **5**, the total energies of molecules computed by HF and DFT methods are lower with about one order of magnitude than the total energies calculated by semiempirical methods (PM3, PM6 and PM7). This can be explained by the fact that semiempirical methods use a simpler Hamiltonian along with empirical data to approximate the Schrödinger equation, and thus treating only the valence electrons. In turn, the core electrons are considered frozen. In contrast, HF and DFT methods treat more precisely all type of electrons, i.e. core and valence electrons. Therefore, the number of double occupied molecular orbitals taken into account by HF and DFT methods is always greater than that considered by semiempirical models (**Tables 4, 5**).

The heats of formation computed by semiempirical methods for the titled compounds **1** and **2** are summarized in **Table B7** (ESI). According to PM3 method, the heats of formation for **1** and **2** were equal to –144.37 kcal/mol and –156.14 kcal/mol, respectively. Other semiempirical techniques (i.e. PM6 and PM7) converged to similar results. The theoretical calculations revealed significant values of the dipole moment for the investigated compounds (**Tables 4** and **5**). For the molecule **1**, the dipole moment ranged from 4.131 to 6.093 Debyes, whereas for the molecule **2**, the calculated dipole moment varied in the extent 3.645–5.674 Debyes, depending on the quantum chemistry method applied. Thus, the dipole moment values for compound **2** are lower than for the compound **1**, due to additional content of hydrophobic (–CH_2–) groups. The calculated polarizability volumes of titled compounds **1** and **2** were found to be equal to 23.28 Å^3 and 26.95 Å^3, respectively. The molecular size (d_{max}) is given in **Tables 4** and **5** as the measure of the maximum atomic distance in the molecules. For instance, according to DFT method, the molecular dimensions for the compounds **1** and **2** are equal to 11.967 Å and 13.946 Å, respectively. The molecular surface area (S_m) and molecular volume (V_m) have been calculated by numerical integration grid techniques implemented in HyperChem program. The calculated values of these parameters are also reported in **Tables 4** and **5.**

The energy spectra of molecular orbitals (MOs) in ground state (S_0) were computed for both molecules by means of quantum chemistry methods. **Figure 7** shows as an example the energy spectra of MOs calculated for the compounds **1** and **2** at the level of PM3 model. As shown in **Figure 7**, each molecular orbital has an orbital index (Ψ_j) and a corresponding energy value (E_j – eigenvalue).

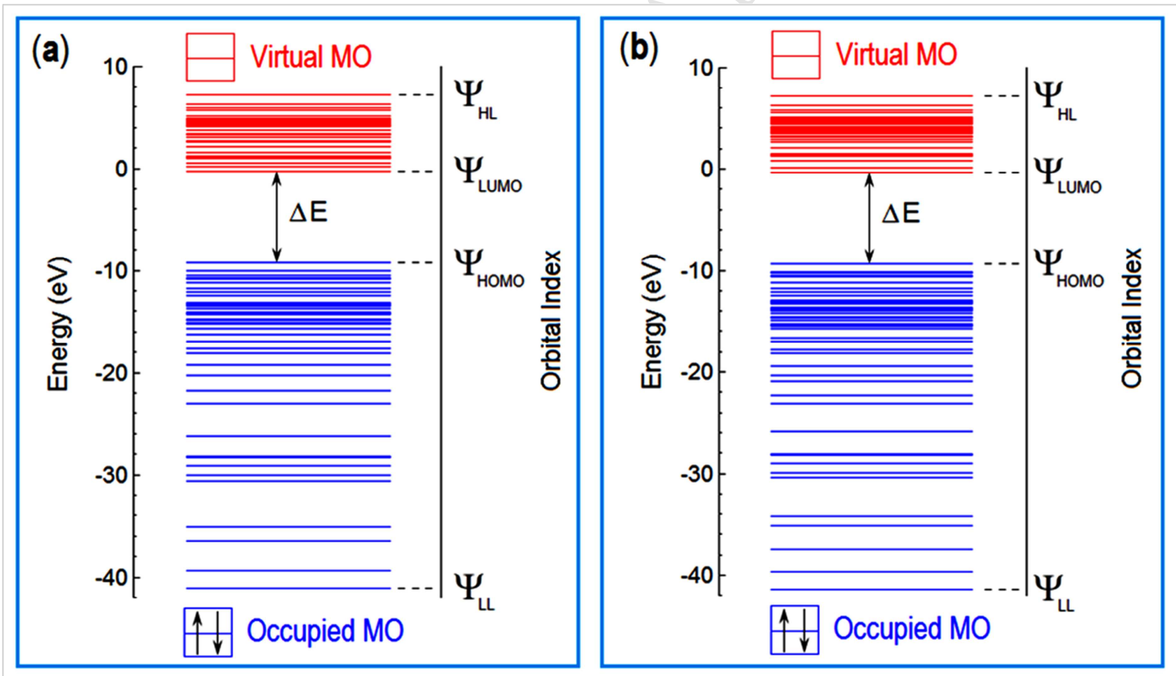

Figure 7. Energy spectra of molecular orbitals (eigenvalues profiles) computed by PM3 method for the investigated molecules **1** (a) and **2** (b) in their ground state (S_0).

Here, the blue lines indicate the eigenvalues of occupied molecular orbitals (OMO), and the red ones denote the energy levels of unoccupied (virtual) orbitals (UMO). Such spectra give useful details about the energy values of the main molecular orbitals. The information about highest occupied (HOMO) and lowest unoccupied (LUMO) molecular orbitals are important, since they are mostly responsible for the chemical reactivity and spectroscopic properties of the molecule [36, 41].

Likewise, the energy difference between frontier molecular orbitals (HOMO-LUMO), known as energy gap (ΔE), is a measure of the intramolecular charge transfer and is frequently used in chemical and biochemical activity studies [42].

The energy values of frontier molecular orbitals (HOMO, LUMO, HOMO–1, LUMO+1) and the corresponding energy gaps (ΔE, ΔE_1) computed by different quantum chemistry methods are summarized in **Tables 4** and **5**. Thus, the semiempirical and HF methods suggested high energy gap (ΔE) values for the titled compounds, i.e. from 8.8 to 10.2 eV. The DFT method provided smaller energy gap values of about 5.1 eV. Such disparity can be attributed to the fact that DFT method (B3LYP/6–31+G**) uses the exchange–correlation functional [43] and therefore it treats in explicit manner the electronic correlation effects comparing with HF and semiempirical methods.

In our case, the large HOMO–LUMO gaps (> 5 eV) suggest the high excitation energies for many excited states, good chemical stability and moderate reactivity for the investigated compounds. The molecular descriptors such as ionization potential (IP), electron affinity (EA), electronegativity (χ), chemical potential (μ), chemical hardness (η) and electrophilicity index (ω) can be computed from the eigenvalues of the frontier molecular orbitals. These estimators are important parameters for quantum chemistry. Note that, electronegativity (χ) is a chemical property describing the tendency of a molecule to attract electrons (or electron density) towards itself. By contrast, the electronic chemical potential (μ) determines the escaping tendency of the electron density from the molecule. The chemical hardness (η) measures the resistance of the molecule to lose electrons. In turn, the electrophilicity index (ω) indicates the electrophilic power of a molecule, its propensity to be saturated with electrons [44].

Thus, by using the energy values of HOMO and LUMO the molecular descriptors have been calculated and reported in **Tables 4** and **5**. The relationships employed for the calculation of the molecular descriptors are given in Ref. [37] and in **Table B8** (ESI). According to the theoretical results, the chemical hardness values greater than 2 eV and the low chemical potential values suggested a good stability and resistance of the molecules to lose electrons. The electronegativity values higher than 3.7 eV indicated the tendency of the molecules to attract the electron density. However, the electrophilicity index values ranging from 1.4 eV to 3.1 eV, revealed a moderate electrophilic power.

The plots of the frontier molecular orbitals for the studied molecules (**1** and **2)** are shown in **Figure 8**. In this figure, the spatial distributions of the molecular orbitals were computed at the level of DFT theory (B3LYP/6–31+G**).

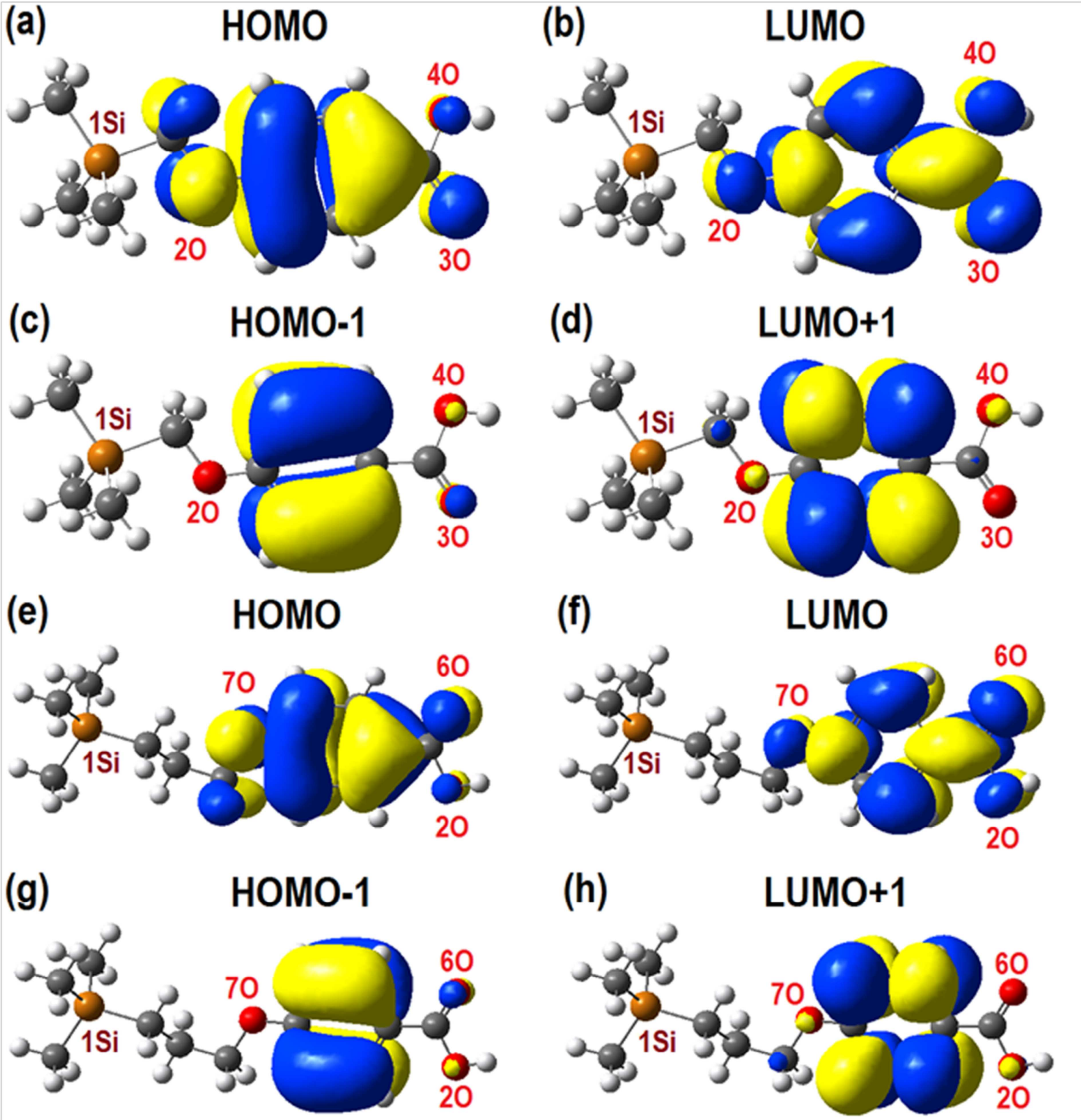

Figure 8. Plots of frontier molecular orbitals for optimized structures of investigated compounds **1** and **2** computed at the level of DFT method (B3LYP/6–31+G**): (a), (b), (c), (d) molecular orbitals for **1**; (e), (f), (g), (h) molecular orbitals for **2.**

As one can see from **Figure 8 (a, e)**, the HOMO is a delocalized π–orbital distributed on the aromatic ring and over the ether and carboxylic groups. By contrast, the HOMO–1 levels

(**Figure 8 c, g**) are localized on the aromatic ring (π–system). The virtual orbitals (LUMO and LUMO+1) are smaller in size than the occupied molecular orbitals. The LUMO lobes are spread on benzene ring and over the ether and carboxylic groups (**Figure 8 b, f**). Hence, LUMO represents a delocalized π*–orbital. The levels of LUMO+1 are localized onto the aromatic ring (**Figure 8 d, h**).

4.3. Charge distribution and electrostatic potential

The charges distribution in a molecule play a key role, since, the partial atomic charges influence many molecular properties such as the electrostatic potential, dipole moment, molecular polarizability, vibrational spectra as well as the acidity-basicity behavior [45,46]. In this work, the atomic charges for the compounds under investigation have been computed using different levels of quantum chemistry theory. The partial atomic charges values for the molecules **1** and **2** are explicitly summarized in **Table B9** and **Table B10** (ESI), respectively. **Figure 9 (a, c)** shows the atomic charges distribution in the molecules **1** and **2**. In this figure, the Mulliken atomic charges were calculated at the level of B3LYP/6–31+G** theory. As one can see, the highest positive charge is attributed to Si–atom followed by C–atom from carboxylic group. The significant negative charges are assigned to oxygen heteroatoms as well as to carbon atoms from silyl group. All hydrogen atoms have slight positive charges, excepting the hydrogen from carboxylic group, which has a higher positive charge. The non–uniform distribution of positive and negative charges on the various atoms in a molecule results in a molecular dipole moment that can be depicted as a vector in three dimensions. The direction of the molecular dipole moment depends on the centers of positive and negative charges. Therefore, it can be used as a descriptor to illustrate the charge movement across the molecule [45]. For the studied molecules **1** and **2**, the orientations of the dipole moments are illustrated as vectors in **Figure 9 (a, c).** The origin of each vector is located near the oxygen atom from ether group and the vector is oriented toward the silyl group. Thus, the dipole moments act in the directions of these vectors quantities, suggesting the polar properties of the investigated compounds **1** and **2**.

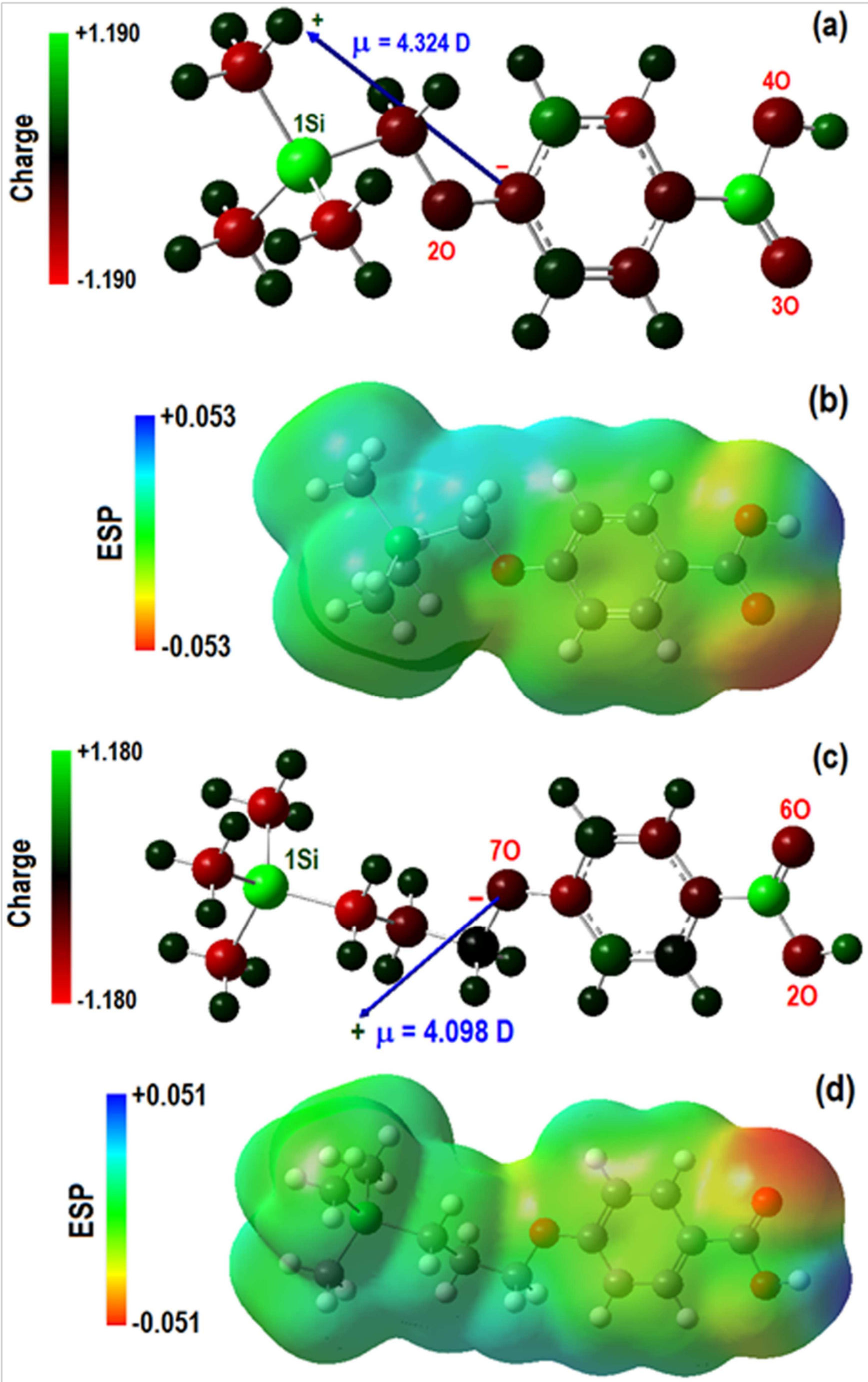

Figure 9. Atomic charges distributions along with dipole moments orientations and electrostatic potential surfaces for the investigated compounds **1** and **2**; computations performed at the level of DFT theory (B3LYP 6–31+G**): (a) atomic charge distribution for **1**; (b) electrostatic potential map for **1**; (c) atomic charge distribution for **2**; (d) electrostatic potential map for **2**.

The molecular electrostatic potential map represents a useful three dimensional diagram to visualize the charge related properties of a molecule. Such maps have been applied extensively to predict the reactive sites for electophilic and nucleophilic attack, as well as to study the biological recognition and hydrogen bonding interactions [46]. On the basis of partial atomic charges, the *electrostatic potential surface* (ESP) surrounding each molecule has been mapped by using the grid–points technique implemented in GaussView 5 program. **Figure 9 (b, d)** illustrates the three–dimensional (3D) mapped isosurfaces of the electrostatic potentials (computed by DFT method) for the molecules **1** and **2**. The red colors denote negative ESP regions followed by green and blue colors indicating neutral and positive ESP domains, respectively. For both molecules **1** and **2**, the oxygen atom from carbonyl group had the highest negative ESP region followed by the oxygen atom from hydroxyl group. These negative ESP areas indicated the sites for electrophilic attack. The most positive ESP region (site of nucleophilic attack) was localized over hydrogen atom from carboxylic group (**Figure 9 b, d**). These theoretical results are in good agreement with the experimental data from X–ray crystallography. Thus, the sites of electrophilic and nucleophilic attack identified by ESP computation corroborate the formation in the crystals of the dimer supramolecular structures by hydrogen–bonding.

4.4. Electronic absorption spectra

The electronic absorption spectrum of a molecule results from the transitions between electronic states of different quantum numbers induced by electromagnetic radiation with ultraviolet or visible (UV–Vis) light [47]. The theoretical absorption spectra are important to reveal the electronic transitions, excitation energies and oscillator strengths [48]. Such spectra provide useful information about intrinsic electronic structure of a molecule. Nowadays, the time–dependent density functional theory (TD–DFT) has become a modern method to determine the electronic excited states for the medium–sized molecular systems (up to 100 atoms) [49].

In this work, TD–DFT approach has been employed to predict the electronic absorption spectra for the investigated compounds **1** and **2**. To this end, the gas–phase optimized geometries (computed at ground–state DFT/ B3LYP/6–31+G** level) have been applied for TD–DFT single–point energy calculations. The TD–DFT computations were performed by means of Gaussian 09 program, taking into account the 10 lowest spin–allowed singlet–singlet electronic transitions. The theoretical absorption spectra for molecules **1** and **2** were simulated in gas–phase as well as in implicit solvents (i.e. DMSO and $CHCl_3$). The implicit solvent calculations were carried out using the *polarizable continuum model* (PCM) with the integral equation formalism (IEFPCM). The theoretical results were compared with the observed UV–Vis spectra experimentally determined for the compounds **1** and **2** in diluted solutions of DMSO and $CHCl_3$ solvents.

The experimental and calculated electronic absorption spectra of the titled compounds are shown in **Figure 10** (for DMSO solvent) and in **Figure A4/**ESI (for $CHCl_3$ solvent).

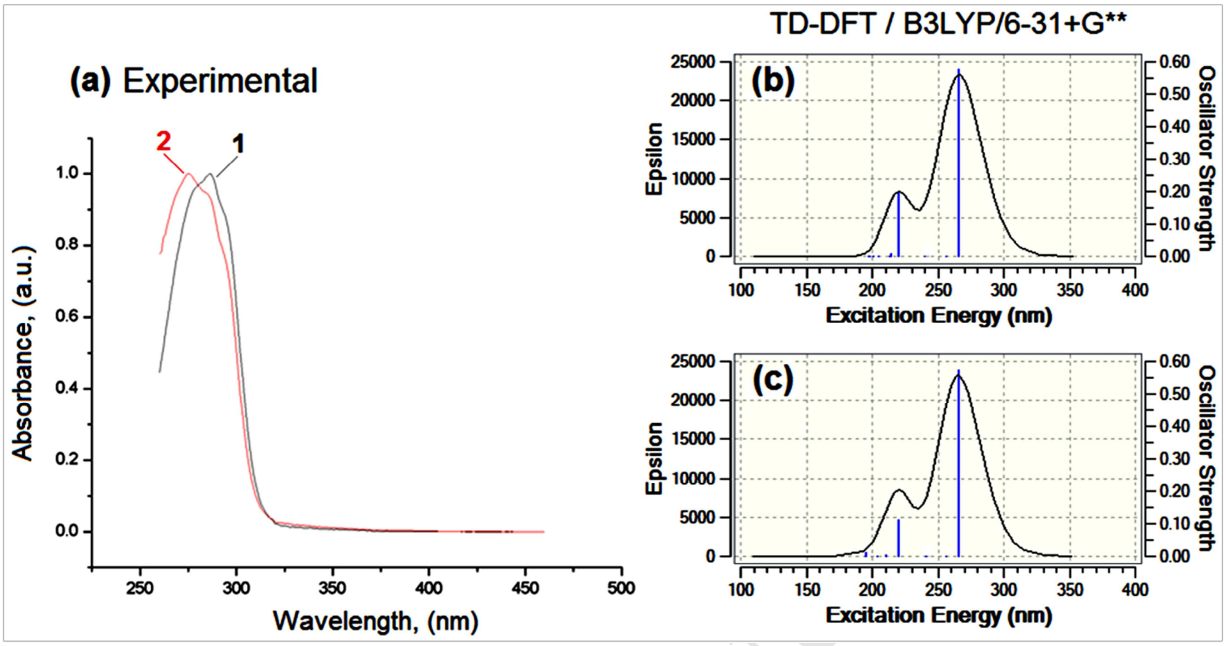

Figure 10. UV–Vis spectra of the investigated compounds in DMSO solvent; (**a**) Experimental UV–Vis spectra for the compounds **1** and **2**; (**b**) Theoretical electronic absorption spectrum (TD–DFT) for the compound **1**; (**c**) Theoretical electronic absorption spectrum (TD–DFT) for the compound **2**.

Table 6 summarizes the values of maximum absorption wavelengths (λ, nm), excitation energies (E,eV) and oscillator strengths (*f*) as well as the main assignments. According to the data reported in **Table 6**, the compound **1** showed a maximum absorption peak (experimental value) at 287 nm (in DMSO) and 285 nm (in $CHCl_3$). The theoretical results (TD–DFT) for the molecule **1** predicted a maximum absorption at lower wavelengths equal to 266 nm (in DMSO) and 265 nm (in $CHCl_3$). Thus, the predicted wavelengths were blue–shifted (hypsochromic effect) with 20–21 nm compared with experimental values. For the molecule **2**, the observed spectral band position in absorption was pinpointed at 275 nm (in DMSO) and 272 nm (in $CHCl_3$). For this case (molecule **2**), the TD–DFT simulations also led to shorter theoretical wavelengths for maximum absorptions, which were equal to 266 nm (in DMSO) and 264 nm (in $CHCl_3$). If compared with experimental observations, the results of TD–DFT suggested a less intense hypsochromic effect (blue–shift) of 8–9 nm for the compound **2**.

Table 6. Summary of data related to the observed and theoretical electronic absorption spectra for the investigated compounds **1** and **2** (absorption wavelength, λ (nm); excitation energy, *E* (eV) and oscillator strength, *f*).

Compound / Method	λ (nm)	*E* (eV)	*f*	Assignments (Contributions)
1 / TD-DFT (Gas phase)	256	4.8394	0.4694	HOMO → LUMO (94%); HOMO-1→LUMO+1 (4%)
1 / TD-DFT (DMSO)	266	4.6586	0.5761	HOMO → LUMO (96%); HOMO-1→LUMO+1 (3%)
1 / Experimental (DMSO)	287	4.3200	-	π→π*
1 / TD-DFT ($CHCl_3$)	265	4.6811	0.5792	HOMO → LUMO (96%); HOMO-1→LUMO+1 (3%)
1 / Experimental ($CHCl_3$)	285	4.3500	-	π→π*
2 / TD-DFT (Gas phase)	256	4.8468	0.4720	HOMO → LUMO (94%); HOMO-1→LUMO+1 (4%)
2 / TD-DFT (DMSO)	266	4.6679	0.5717	HOMO → LUMO (96%); HOMO-1→LUMO+1 (3%)
2 / Experimental (DMSO)	275	4.5090	-	π→π*
2 / TD-DFT ($CHCl_3$)	264	4.6903	0.5749	HOMO → LUMO (96%); HOMO-1→LUMO+1 (3%)
2 / Experimental ($CHCl_3$)	272	4.5580	-	π→π*

The hypsochromic effects for gas phase were more significant than those for implicit solvents. The maximum absorption peaks that ranged from 256 nm to 287 nm have been assigned to the $\pi \rightarrow \pi^*$ electronic transitions. The TD–DFT theory revealed that these excited states belong to HOMO→LUMO and HOMO–1→LUMO+1 electronic transfer. The excited electronic configuration HOMO→LUMO has a major contribution (94–96%), whereas HOMO–1→LUMO+1 has a minor contribution (3–4%). The contributions of the excited electronic states were calculated based on the values of coefficients of the specific configurations. To this end, the open–source software GaussSum 3.0 [50,51] has been employed, which was developed for analyzing the output files from several computational chemistry packages. Hence, the theoretical results suggested that the π electronic system delocalized over the aromatic ring, ether and carboxylic groups (**Figure 8**) was mainly responsible for the maximum absorption peaks of the compounds **1** and **2**.

In summary, both observed and theoretical UV–Vis spectra showed maximum absorption peaks located into the near–ultraviolet region (256–287 nm) that were assigned to $\pi \rightarrow \pi^*$ electronic transitions. Thus, the experimental UV–Vis spectra for **1** and **2** were in reasonable agreement with the theoretical electronic absorption spectra computed by TD–DFT method.

4.5. Vibrational spectra

The infrared (IR) spectrum reveals the vibrations of atoms within a molecule giving useful information about various functional groups. Due to the characteristic vibration frequencies of certain groups of atoms, the spectrum provides the relationship between infrared bands and the molecular structure. The experimental and predicted IR spectra of the studied compounds are shown in **Figure 11**. In this figure, the theoretical infrared vibrational frequencies (scaled) and intensities were calculated by DFT/B3LYP/6–31+G** method. The detailed vibrational analyses of fundamentals modes computed by B3LYP/6–31+G** method are listed in ESI, i.e. **Table B11** (for **1**) and **Table B12** (for **2**). These tables report the calculated wavenumbers (unscaled and scaled values), IR intensities, reduced masses, force constants as well as the mode assignments of IR absorption bands. As given in **Tables B11–B12** (ESI), the DFT theory provided 87 and 105 vibration modes for the compounds **1** and **2**, respectively.

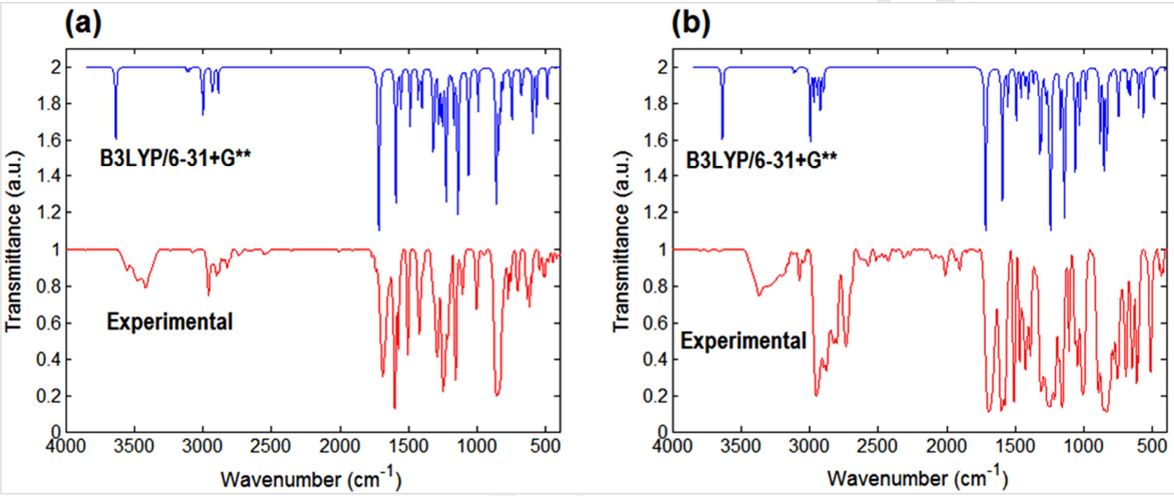

Figure 11. IR spectra of the investigated compounds: experimental vs. theoretical (B3LYP/6–31+G**); (a) IR spectra for the compound **1**; (b) IR spectra for the compound **2**.

The vibrational frequencies provided by quantum chemistry programs are often multiplied by a scale factor (in the range of 0.8 to 1.0) to better match the experimental vibrational frequencies. In this study, the scaled wavenumbers were calculated by multiplying the unscaled values with a factor of 0.964 (for B3LYP/6–31+G**) according to the NIST computational chemistry comparison and benchmark database [52]. Such scaling procedure compensates for several issues, i.e. the electronic structure calculation is approximate; the potential energy surface is not harmonic and the intermolecular interactions are ignored [52].

The assignments for the calculated wavenumbers were aided by the animation option of the GaussView–5 program, which provided a visual presentation of the vibration modes [32]. Many theoretical vibration modes involved the coupled movements of atoms from different groups presented in the molecule (see ESI, **Tables B11–B12**).

For the experimental FTIR spectra, the main assignments were attributed in accordance with the literature data [53] and were summarized in **Table 7,** for both compounds **1** and **2**.

Table 7. Observed vibrational frequencies and the corresponding main assignments for the investigated compounds **1** and **2**.

Functional Groups	Group frequency, wavenumber (cm^{-1})		Main assignment
	1 ($C_{11}H_{16}O_3Si$)	**2** ($C_{13}H_{20}O_3Si$)	
$–(CH_2)_n–$ n=1 or 3	2957, 2901	2951, 2895	υ_a (C–H)
	2822	2877	υ_s (C–H)
Aromatic (C–H)	3074	3077	υ (C–H) (aromatic ring)
	775	786	γ (C–H) (aromatic ring)
Aromatic (C=C–C)	1601, 1572, 1506	1605, 1578, 1510	υ (C=C–C) (aromatic ring)
Ether group (C–O–C)	1292	1313	υ_a (C–O–C)
	1157	1159	υ_s (C–O)
Carboxylic acid (O–H)	3416	3366	υ_s (O–H)
	1421	1427	β O–H
Carboxylic acid (C=O)	1688	1693	υ_s (C=O)

$(CH_3)_3$–Si–CH_2–	1250	1250	υ (Si–C) + γ (C–H)
	858	835	υ (Si–C)

υ: stretching vibration (s – sym.; a –asym.); β: in–plane bending; γ: out–of–plane bending.

The experimental FTIR spectra recorded in the 400–4000 cm^{-1} region showed the characteristic bands of stretching vibrations (υ) of the following groups: C–H, C–O–C, O–H, C=O, Si–C and C=C–C (aromatic ring). For details, see **Table 7**.

Thus, the stretching vibrations υ(C–H) from aliphatic groups have been observed in the region 2822–2957 cm^{-1}. The aliphatic υ(C–H) vibrations were predicted by DFT method at wavenumbers (scaled values) ranging from 2888 to 3008 cm^{-1} (see ESI, **Tables B11–B12**). The stretching vibrations υ(C–H) for the aromatic ring were determined experimentally at 3074 cm^{-1} and 3077 cm^{-1}, for the compounds **1** and **2**, respectively. The theoretical counterparts for υ(C–H) (aromatic ring) were predicted by DFT in the range 3090–3117 cm^{-1}.

The symmetric stretching of O–H bond from carboxyl group was observed at 3416 cm^{-1} and 3366 cm^{-1} for the compounds **1** and **2**, respectively. The calculated wavenumber for υ_s(O–H) was pinpointed at 3635 cm^{-1} in both cases. The O–H bending vibrations were observed within the range 1421–1427 cm^{-1} and predicted in the region 1313–1406 cm^{-1}. The strong signals identified experimentally at 1688 cm^{-1} (for **1**) and 1693 cm^{-1} (for **2**) were assigned to symmetrical C=O stretching bands. The theoretical vibration υ_s(C=O) was found at 1718 cm^{-1} (for **1** and **2**).

In both molecules, the stretching vibrations of C=C–C from aromatic ring appeared in the range 1506–1605 cm^{-1} with the intensities varying from medium to strong. The DFT computations provided the modes for υ(C=C–C / aromatic ring) in the region 1489–1595 cm^{-1}.

Regarding the ether group, the C–O–C asymmetric stretching oscillation was assigned to the frequency observed at 1292 cm^{-1} (for **1**) and 1313 cm^{-1} (for **2**). The vibration υ_a(C–O–C) was identified theoretically at 1227 cm^{-1} (only for the compound **1**). According to the experimental data, the signals positioning at 1157 cm^{-1} and 1159 cm^{-1} were attributed to the C–O symmetric stretching vibrations. The DFT calculations provided the modes for υ_s(C=O) at 994–1063 cm^{-1}.

According to the experimental FTIR spectra, the stretching oscillation Si–C was recognized by the bands at 1250 cm^{-1} along with the strong peaks in the region 835–858 cm^{-1}. The predicted modes for υ(Si–C) appeared at the ranges 1169–1238 cm^{-1} and 836–861 cm^{-1}. The medium bands observed at wavelength 775 cm^{-1} (for **1**) and 786 cm^{-1} (for **2**) were assigned to the out–of–plane bending vibrations of C–H from the aromatic ring.

In addition, the theoretical IR spectra were computed at the level of HF/6–31+G**, PM3, PM6 and PM7 methods and were shown for comparison in **Figure A5** (ESI). In order to estimate the goodness–of–fit between experimental and theoretical vibration frequencies, the linear correlation coefficients (r^2) were calculated and reported in **Table B13** (ESI). According to these data, the greatest values of correlation coefficients were provided by B3LYP/6–31+G** method, and were equal to 0.9972 and 0.9971, for the compounds **1** and **2**, respectively (**Table B13**). Thus, the DFT yielded a better correlation between experimental and calculated vibration frequencies than other computational chemistry methods applied in this work.

The parity plots between experimental wavenumbers and theoretical (scaled) counterparts computed by B3LYP/6–31+G** method are illustrated in **Figure 12** for the investigated compounds **1** (**Figure 12 a**) and **2** (**Figure 12 b**). As shown in **Figure 12**, the linear correlations emerge between observed and predicted vibrational frequencies (r^2>0.997). The linear regression lines almost overlap with bisectors for the lower range 500–1700 cm^{-1}. For the higher region

2500–3500 cm^{-1}, a minor disparity between strait lines and bisectors can be distinguished. Overall, most of data were scattered nearby the bisectors revealing a good agreement between observed and predicted wavelengths. Hence, both experimental and theoretical vibrational spectra provided adequate relationships between infrared bands and the molecular structures.

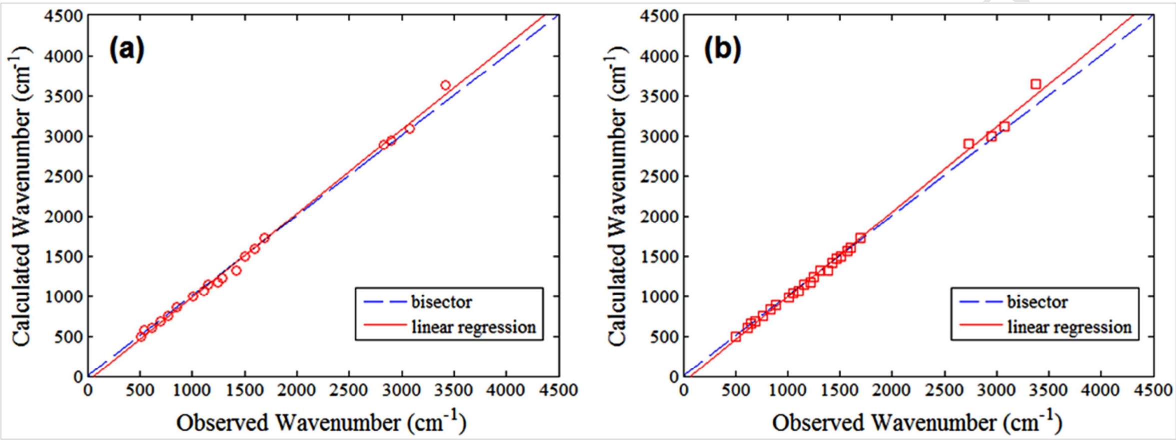

Figure 12. Parity plots between experimental and theoretical (scaled) wavenumbers; (**a**) parity plot for the compound **1**; (**b**) parity plot for the compound **2**; theoretical vibrational frequencies calculated by B3LYP/6–31+G** method.

5. Conclusions

Two silicon–containing organic compounds, namely 4–((trimethylsilyl)methoxy) and 4–(3–(trimethylsilyl)propoxy)benzoic acids (**1** and **2**) were synthesized for the first time. The compounds were characterized by X–ray single–crystal diffraction, ^{1}H NMR, ^{13}C NMR and FTIR spectroscopy techniques. Structural data were complemented with quantum chemical computations using DFT/B3LYP/6–31+G**, HF/6–31+G** as well as semi empirical (PM3, PM6 and PM7) methods. Theoretical optimized geometries for the investigated molecules were in good agreement with our reported X–ray structures.

The calculated partial atomic charges and dipole moments (4–6 Debye) suggested the polar properties of the investigated compounds. The mapped electrostatic potential surfaces revealed the sites for electrophilic and nucleophilic attack localized near the carboxylic group, on oxygen and hydrogen atoms, respectively. These sites identified theoretically corroborated the observation of the dimer supramolecular structures formed in the crystals by hydrogen–bonding. The calculated HOMO–LUMO gaps (ΔE) greater than 5 eV suggested good chemical stability and moderate reactivity for the investigated compounds.

Theoretical electronic absorption spectra were developed using TD–DFT method and compared with experimental UV–Vis spectra. A reasonable agreement between experimental and theoretical electronic spectra was concluded. Both observed and theoretical UV–Vis spectra indicated the maximum absorption peaks pinpointed at 256–287 nm (near–ultraviolet region) that were assigned to $\pi \rightarrow \pi^*$ electronic transitions. The theory (TD–DFT) suggested that the π electronic system delocalized over the aromatic ring, ether and carboxylic groups was mainly responsible for the most intense transition bands for the investigated compounds **1** and **2**.

The theoretical vibrational band assignments were performed at the level of DFT B3LYP/6–31+G** model in order to compare the experimental (FTIR) and calculated vibrational frequencies. The infrared spectra showed the characteristic bands of stretching vibrations of the following groups: C–H, C–O–C, O–H, C=O, Si–C and C=C–C (aromatic ring). The results revealed a good agreement between observed and predicted infrared wavenumbers. Both experimental and theoretical vibrational spectra provided adequate relationships between infrared bands and the molecular structures of the studied compounds.

Acknowledgement

This research was founded by the Romanian Ministry of National Education under Grant 53/02.09.2013, Cod: PN-II-ID-PCE-2012-4-0261. The author Corneliu Cojocaru acknowledges the Project SupraChem Lab, Horizon 2020 WIDESPREAD 2-2014: ERA Chairs, Project no. 667387.

Supporting Information

1D supramolecular aggregation in the crystal structure of **1,** tables containing bonds lengths (Å), interatomic angles (^{o} deg), dihedral angles for the molecules **1** and **2,** Superposition of the X–ray structure of **1** and **2** and the corresponding optimized counterparts computed by different QM methods, tables containing heats of formation (H_f, kcal/mol) for **1** and **2** calculated by semiempirical methods and the relationships used for calculation of the molecular descriptors, tables containing partial atomic charges for the molecule **1** and **2**, calculations done by different methods, experimental and theoretical UV–Vis spectra of the investigated compounds, tables containing predicted vibrational frequencies (ν, cm^{-1}), IR intensities (*IR*, km/mole), reduced mass (*RM*, a.m.u), force constants (*FC*, mDyne/Å) and assignments computed by B3LYP/6–31+G** method for the compounds **1** and **2,** plots of theoretical IR spectra calculated by different computational chemistry methods, tables containing linear correlation coefficient (r^2) between experimental IR–wavenumbers and calculated frequencies, given by different quantum chemistry methods, ^{1}H NMR and ^{13}C NMR spectra of the compounds **1** and **2** are provided.

References

[1] H.B. Guo, F. He, B. Gu, L. Liang, J.C. Smith, Time-dependent density functional theory assessment of UV absorption of benzoic acid derivatives, J. Phys. Chem. A 116 (2012) 11870–11879.

[2] M. Karabacak, Z. Cinar, M. Kurt, S. Sudha, N. Sundaraganesan, FT-IR, FT-Raman, NMR and UV–vis spectra, vibrational assignments and DFT calculations of 4-butyl benzoic acid, Spectrochim. Acta A 85 (2012) 179–189.

[3] S.P. Verevkin, D.H. Zaitsau, V.N. Emelyanenko, E.N. Stepurko, K.V. Zherikova, Benzoic acid derivatives: Evaluation of thermochemical properties with complementary experimental and computational methods, Thermochim. Acta 622 (2015) 18–30.

[4] V. Balachandran, V. Karpagam, G. Santhi, B. Revathi, G. Ilango, M. Kavimani, Conformational stability, vibrational (FT-IR and FT-Raman) spectra and computational analysis of *m*-trifluoromethyl benzoic acid, Spectrochim. Acta A 137 (2015) 165–175.

[5] M. Kurt, E. Babur Sas, M. Can, S. Okur, S. Icli, S. Demic, M. Karabacak, T. Jayavarthanan, N. Sundaraganesan, Synthesis and spectroscopic characterization on 4-(2,5-di-2-thienyl-1H-pyrrol-1-yl)benzoic acid: A DFT approach, Spectrochim. Acta A 152 (2016) 8–17.

[6] V. Balachandran, S. Lalitha, S. Rajeswari, V.K. Rastogi, Theoretical investigations on the molecular structure, vibrational spectra, thermodynamics, HOMO–LUMO, NBO analyses and paramagnetic susceptibility properties of p-(p-hydroxyphenoxy)benzoic acid, Spectrochim. Acta A 121 (2014) 575–585.

[7] P.D.S. Babu, S. Periandy, S. Ramalingam, Vibrational spectroscopic (FTIR and FTRaman) investigation using ab initio (HF) and DFT (LSDA and B3LYP) analysis on the structure of Toluic acid, Spectrochim. Acta A 78 (2011) 1321–1328.

[8] M. Cinar, N. Yildiz, M. Karabacak, M. Kurt, Determination of structural, spectrometric and nonlinear optical features of 2-(4-hydroxyphenylazo)benzoic acid by experimental techniques and quantum chemical calculations, Spectrochim. Acta A 105 (2013) 80–87.

[9] N. Balamurugan, C. Charanya, S. SampathKrishnan, S. Muthu, Molecular structure, vibrational spectra, first order hyper polarizability, NBO and HOMO–LUMO analysis of 2-amino-5-bromo-benzoic acid methyl ester, Spectrochim. Acta A 137 (2015) 1374–1386.

[10] M. Szafran, A. Katrusiak, Z. Dega-Szafran, I. Kowalczyk, The structure of 4-(trimethylammonium)benzoic acid chloride studied by X-ray diffraction, DFT calculations, NMR and FTIR spectroscopy, J. Mol. Struct. 996 (2011) 75–81.

[11] V. Mukherjee, N.P. Singh, R.A. Yadav, Experimental and calculation aspects of vibrational spectra and optimized geometry of 2,3,4-tri-fluoro-benzoic acid dimer, Spectrochim. Acta A 74 (2009) 1107–1114.

[12] S. Muthu, E. IsacPaulraj, Spectroscopic and molecular structure (monomeric and dimeric structure) investigation of 2-[(2-hydroxyphenyl) carbonyloxy] benzoic acid by DFT method: A combined experimental and theoretical study, J. Mol. Struct. 1038 (2013) 145–162.

[13] S.L. Chen, Z. Liu, J. Liu, G.C. Han, Y.H. Li, Synthesis, characterization, crystal structure and theoretical approach of Cu(II) complex with 4-{(Z)-[(2-hydroxybenzoyl)hydrazono]methyl} benzoic acid, J. Mol. Struct. 1014 (2012) 110–118.

[14] A.D. Marinkovic, B.Z. Jovanovic, F.H. Assaleh, V.V. Vajs, M. I. Juranic, Linear free energy relationships applied to the reactivity and the ^{13}C NMR chemical shifts in 4-[[(substituted phenyl)imino]methyl]benzoic acids, J. Mol. Struct. 1011 (2012) 158–165.

[15] F. Montilla, V. Rosa, C. Prevett, T. Avilés, M. Nunes da Ponte, D. Masi, C. Mealli, Trimethylsilyl-substituted ligands as solubilizers of metal complexes in supercritical carbon dioxide, Dalton Trans. (2003) 2170–2176.

[16] T. Kawamoto, A. Tanaka, Enzymatic Conversion of Organosilicon Compounds in Organic Solvents, in: Enzymes in Nonaqueous Solvents: Methods and Protocols by E.N. Vulfson, P.J. Halling, (2001), Humana Press Inc., Totowa, New Jersey, United States, pp.345.

[17] R.W. Bott, C. Eaborn, P.W. Jones, Organosilicon compounds. XXXVIII. The preparation and optical resolution of *p*-[ethylmethyl(*p*-methoxyphenyl)silyl]benzoic acid, J. Organomet. Chem. 6 (1966) 484–489.

[18] A. Furstner, I. Konetzki, Synthesis of 2-hydroxy-6-{[(16*R*)-β-δ-mannopyransyloxy]heptadecyl}benzoic acid, a fungal metabolite with $GABA_A$ ion channel receptor inhibiting properties, Tetrahedron 52 (1996) 15071–15078.

[19] J.M. Weinberg, K.L. Wooley, The investigation of a transsilylation reaction for the preparation of silyl esters: reactivity correlated with ^{29}Si NMR resonance frequencies, J. Organomet. Chem. 542 (1997) 235–240.

[20] W. Bains, R. Tacke, Silicon chemistry as a novel source of chemical diversity in drug design, Curr. Opin. Drug. Discov. Devel. 6 (2003) 526–543.

[21] X. Steinberg, C. Lespay-Rebolledo, S. Brauchi, A structural view of ligand-dependent activation in thermo TRP channels, Front. Physiol. 5 (2014) Article 171.

[22] CrysAlis RED, Oxford Diffraction Ltd., Version 1.171.36.32, (2003).

[23] O.V. Dolomanov, L.J. Bourhis, R.J. Gildea, J.A.K. Howard, H. Puschmann, J. Appl. Cryst. 42 (2009) 339‒341.

[24] G. M. Sheldrick, SHELXS, Acta Cryst. A64 (2008) 112‒122.

[25] M.J. Frisch, G.W. Trucks, H.B. Schlegel, G.E. Scuseria, M.A. Robb, J.R. Cheeseman, G. Scalmani, V. Barone, B. Mennucci, G.A. Petersson, H. Nakatsuji, M. Caricato, X. Li, H.P. Hratchian, A.F. Izmaylov, J. Bloino, G. Zheng, J.L. Sonnenberg, M. Hada, M. Ehara, K. Toyota,

R. Fukuda, J. Hasegawa, M. Ishida, T. Nakajima, Y. Honda, O. Kitao, H. Nakai, T. Vreven, J.A. Montgomery, J.E. Peralta, F. Ogliaro, M. Bearpark, J.J. Heyd, E. Brothers, K.N. Kudin, V.N. Staroverov, R. Kobayashi, J. Normand, K. Raghavachari, A. Rendell, J.C. Burant, S.S. Iyengar, J. Tomasi, M. Cossi, N. Rega, J.M. Millam, M. Klene, J.E. Knox, J.B. Cross, V. Bakken, C. Adamo, J. Jaramillo, R. Gomperts, R.E. Stratmann, O. Yazyev, A.J. Austin, R. Cammi, C. Pomelli, J.W. Ochterski, R.L. Martin, K. Morokuma, V.G. Zakrzewski, G.A. Voth, P. Salvador, J.J. Dannenberg, S. Dapprich, A.D. Daniels, Ö. Farkas, J.B. Foresman, J.V. Ortiz, J. Cioslowski, D.J. Fox, Gaussian 09. *Gaussian*. Inc., Wallingford CT, (2009). Official Website: http://www.gaussian.com/.

[26] J.J.P. Stewart, MOPAC 2012, Stewart Computational Chemistry, Version 14.139W, (2012), Colorado Springs, Website: http://openmopac.net.

[27] J.J.P. Stewart, MOPAC: A semiempirical molecular orbital program, J. Comp. Aided Mol. Des. 4 (1990) 1–103.

[28] J.D.C. Maia, G.A.U. Carvalho, C.P. Mangueiram, S.R. Santana, L.A.F. Cabral, G.B. Rocha, GPU linear algebra libraries and GPGPU programming for accelerating MOPAC semiempirical quantumchemistry calculations, J. Chem. Theory Comput. 8 (2012) 3072–3081.

[29] J.J.P. Stewart, Optimization of parameters for semiempirical methods I. Method, J. Comput. Chem. 10 (1989) 209–220.

[30] J.J.P. Stewart, Optimization of parameters for semiempirical methods V: Modification of NDDO approximations and applications to 70 elements, J. Mol. Model. 13 (2007) 1173–1213.

[31] J.J.P. Stewart, Optimization of parameters for semiempirical methods VI: more modifications to the NDDO approximations and re-optimization of parameters, J. Mol. Model. 19 (2013) 1–32.

[32] R. Dennington, T. Keith, J. Millam, GaussView, Version 5, Semichem Inc., Shawnee Mission, KS. (2009). Website: http://www.gaussian.com/g_prod/gv5.htm.

[33] A.R. Allouche, Gabedit – A graphical user interface for computational chemistry softwares, J. Comput. Chem. 32 (2011) 174–182.

[34] *HyperChem (TM) Release 8.0,* Hypercube, Inc., 1115 NW 4th Street, Gainesville, Florida 32601, USA, Website: http://www.hyper.com/.

[35] H. Bernhard Schlegel, Geometry optimization, WIREs Comput. Mol. Sci. 1 (2011) 790–809.

[36] C. Cojocaru, A. Rotaru, V. Harabagiu, L. Sacarescu, Molecular structure and electronic properties of pyridylindolizine derivative containing phenyl and phenacyl groups: Comparison between semi-empirical calculations and experimental studies, J. Mol. Struc. 1034 (2013) 162–172.

[37] C. Cojocaru, A. Airinei, N. Fifere, Molecular structure and modeling studies of azobenzene derivatives containing maleimide groups, Springer Plus 2 (2013) 1–19.

[38] C.T. Zeyrek, H. Unver, O.T. Arpaci, K. Polat, N.O. Iskeleli, M. Yildiz, Experimental and theoretical characterization of the 2-(4-bromobenzyl)-5-ethylsulphonyl-1,3-benzoxazole, J. Mol. Struc. 1081 (2015) 22–37.

[39] E.G. Saglam, A. Ebinc, C.T. Zeyrek, H. Unver, T. Hokelek, Structural studies on some dithiophosphonato complexes of Ni(II), Cd(II), Hg(II) and theoretical studies on a dithiophosphonato Ni(II) complex using density functional theory, J. Mol. Struc. 1099 (2015) 490–501.

[40] O.M. Becker, Conformational Analysis, in Computational Biochemistry and Biophysics. Eds. Becker, O. M.; MacKerell, A. D.; Roux, B.; Watanabe, M. Publisher Marcel Dekker, New York, (2001), pp. 69-90.

[41] A. Chitradevi, S.S. Kumar, S. Athimoolam, S.A. Bahadur, B. Sridhar, Single crystal XRD, vibrational spectra, quantum chemical and thermal studies on a new semi-organic crystal: 4-Aminium antipyrine chloride, J. Mol. Struct. 1099 (2015) 58–67.

[42] Y.N. Mabkhot, F.D. Aldawsari, S.S. Al-Showiman, A. Barakat, S.M. Soliman, M.I. Choudhary, S. Yousuf, M.S. Mubarak, T.B. Hadda, Novel enaminone derived from [2,3–b] thiene: Synthesis, X-Ray crystal structure, HOMO, LUMO, NBO analyses and biological activity, Chem. Central J. 9 (2015) 1–11.

[43] G. Zhang, C.B. Musgrave, Comparison of DFT methods for molecular orbital eigenvalue calculations, J. Phys. Chem. A 111 (2007) 1554–1561.

[44] R.G. Parr, L.V. Szentpaly, S. Liu, Electrophilicity Index, J. Am. Chem. Soc. 121 (1999) 1922–1924.

[45] I. Sidir, Y.G. Sidir, M. Kumalar, E. Tasal, Ab initio Hartree–Fock and density functional theory investigations on the conformational stability, molecular structure and vibrational spectra of 7-acetoxy-6-(2,3-dibromopropyl)-4,8-dimethylcoumarin molecule, J. Mol. Struc. 964 (2010) 134–151.

[46] A. Barakat, A.M. Al-Majid, S.M. Soliman, Y.N. Mabkhot, M. Ali, H.A. Ghabbour, H.K. Fun, A. Wadood, Structural and spectral investigations of the recently synthesized chalcone (E)-3-mesityl-1-(naphthalen-2-yl) prop-2-en-1-one, a potential chemotherapeutic agent, Chem. Central J. 9 (2015) 1–15.

[47] S. Grimme, Calculation of the electronic spectra of large molecules, Rev. Comput. Chem. 20 (2004) 153–218.

[48] D. Mahadevan, S. Periandy, M. Karabacak, S. Ramalingam, N. Puviarasan, Spectroscopic (FT–IR, FT–Raman and UV–vis) investigation and frontier molecular orbitals analysis on 3-

methyl-2-nitrophenol using hybrid computational calculations, Spectrochim. Acta A 86 (2012) 139–151.

[49] S. Fleming, A. Mills, T. Tuttle, Predicting the UV–vis spectra of oxazine dyes, Beilstein J. Org. Chem. 7 (2011) 432–441.

[50] N.M. O'Boyle, A.L. Tenderholt, K.M. Langner, A library for package-independent computational chemistry algorithms, J. Comput. Chem. 29 (2008) 839–845.

[51] N.M. O'Boyle, GaussSum open-source program, Version 3.0, (2013), available online at http://gausssum.sourceforge.net/.

[52] R.D. Johnson III, NIST Computational Chemistry Comparison and Benchmark Database, NIST Standard Reference Database Number 101, Release 16a, August (2013). CCCBDB III.B.3.a. (XIII.C.1.); Precomputed vibrational scaling factors. Retrieved from web-page: http://cccbdb.nist.gov/vibscalejust.asp.

[53] G. Socrates, Infrared and Raman characteristic group frequencies. Tables and Charts, John Wiley & Sons, LTD, Chichester, 3rd edition (2001) pp. 50–246.

Highlights

- Two original carboxylic acids containing trimethylsilyl tails were obtained and characterized.
- The optimized molecular geometries are in good agreement with X-ray molecular structures.
- The computed vibrational frequencies and electronic absorption spectra were assigned and compared with the experimental FTIR and UV-Vis spectra.